Missouri S&T Library and Learning Resources

Scholars' Mine

Masters Theses

Student Theses and Dissertations

Fall 2020

Characterization of a plasma source simulating solar wind plasma in a vacuum chamber

Blake Anthony Folta

Follow this and additional works at: https://scholarsmine.mst.edu/masters_theses

Part of the Aerospace Engineering Commons, and the Plasma and Beam Physics Commons

Department:

Recommended Citation

Folta, Blake Anthony, "Characterization of a plasma source simulating solar wind plasma in a vacuum chamber" (2020). *Masters Theses*. 7964.
https://scholarsmine.mst.edu/masters_theses/7964

This thesis is brought to you by Scholars' Mine, a service of the Missouri S&T Library and Learning Resources. This work is protected by U. S. Copyright Law. Unauthorized use including reproduction for redistribution requires the permission of the copyright holder. For more information, please contact scholarsmine@mst.edu.

CHARACTERIZATION OF A PLASMA SOURCE SIMULATING SOLAR WIND PLASMA IN A VACUUM CHAMBER

by

BLAKE ANTHONY FOLTA

A THESIS

Presented to the Graduate Faculty of the

MISSOURI UNIVERSITY OF SCIENCE AND TECHNOLOGY

In Partial Fulfillment of the Requirements for the Degree

MASTER OF SCIENCE

in

AEROSPACE ENGINEERING

2020

Approved by

Dr. Daoru Han, Advisor
Dr. Serhat Hosder
Dr. David Riggins

Copyright 2020

BLAKE ANTHONY FOLTA

All Rights Reserved

ABSTRACT

The United States has set an aggressive time line to not only return to the Moon, but also to establish a sustained human presence. In the Apollo missions dust was a significant factor, but the duration of those missions was short so dust and surface charging were problems, but they did not pose an immediate threat. For a long-term mission, these problems instead become incredibly detrimental. Because of this, research needs to be conducted to investigate these phenomena so that mitigation techniques can be developed and tested. To this end, this thesis serves to demonstrate the Gas and Plasma Dynamics Lab's (GPDL) ability to recreate the lunar plasma environment, and to establish competence to conduct meaningful experimental research on this topic. This work may also serve as a guide for future researchers in the GPDL. Further, this work suggests avenues of near-future experimental work, as well as inexpensive improvements to the facility, which will increase the capability of the GPDL in the long term.

ACKNOWLEDGMENTS

I could not have asked for a better graduate school experience. I learned a lot and am very grateful. So many people have helped me along the way.

First and foremost, I would like to thank my advisor Dr. Han. You took me in as a chemical engineering graduate who know almost nothing about the aerospace field, and you patiently helped me along the steep learning curve of this field. I cannot thank you enough for everything you've done for me. Your course on Plasma Physics was helpful for obvious reasons, and your Physical Gas Dynamics course gave me the tools to develop the model in Section 5 of this thesis.

I would also like to thank my committee for taking the time to review this document. Dr. Hosder, the tools I learned from your Applied Computational Methods course were instrumental in this research and helped immensely in other classes. I look forward to reading your body of work as I prepare for hypersonics projects at Eglin AFB. Dr. Riggins, your Advanced Propulsion class is what got my foot in the door at Eglin. Throughout my career, I will do my best to make sure that the exergy assessment methods you have developed are properly utilized by the industry.

To the Mechanical and Aerospace Engineering Department and the Materials Research Center, thank you for the funding provided to the GPDL. I would also like to thank the NASA Missouri Space Grant Consortium for the personal research grant they awarded me, that $3,000 may not have seemed like much, but it went a long way.

So many others have made this possible, too many to include in a single page. To everyone who helped me along the way: thank you, I could not have done this without you. Please find specific notes of my gratitude in Appendix A.

TABLE OF CONTENTS

Page

ABSTRACT iii

ACKNOWLEDGMENTS iv

LIST OF ILLUSTRATIONS viii

LIST OF TABLES x

SECTION

1. INTRODUCTION 1
   - 1.1. MOTIVATION 1
   - 1.2. DUST TRANSPORT 2
   - 1.3. ARCING 3
   - 1.4. OBJECTIVES 4

2. LITERATURE REVIEW 5
   - 2.1. THE LUNAR PLASMA ENVIRONMENT 5
   - 2.2. THE VACUUM CHAMBER PLASMA ENVIRONMENT 6

3. TESTING FACILITY OVERVIEW AND CHARACTERIZATION 9
   - 3.1. GENERAL OVERVIEW 9
   - 3.2. VEECO® RF PLASMA SOURCE OVERVIEW 9
   - 3.3. VACUUM FACILITY OVERVIEW 11
   - 3.4. VACUUM CHAMBER CHARACTERIZATION 12
     - 3.4.1. Experimental Overview 12

3.4.2. Results and Discussion 13

4. PLASMA DIAGNOSTICS 16

4.1. OUTLINE 16

4.2. LANGMUIR PROBES 16

4.2.1. Overview 16

4.2.2. RF Compensation 19

4.2.3. Data Analysis 20

4.2.4. Accounting for Sheath Expansion 25

4.2.5. Uncertainty 26

4.3. FARADAY PROBE 27

4.4. RESULTS 31

4.4.1. Local Plume Properties 31

4.4.2. Ongoing Plume Characterization 35

5. MODELING LOCAL CHARGE EXCHANGE ION DENSITY 37

5.1. REASONING FOR THE MODEL 37

5.2. MODEL INPUTS 38

5.3. MODEL DERIVATION 42

5.4. RESULTS AND DISCUSSION 47

6. SUMMARY, CONCLUSION, AND RECOMMENDED FUTURE WORK 49

6.1. SUMMARY 49

6.2. CONCLUSION 49

6.3. RECOMMENDED FUTURE WORK 50

6.3.1. Experiment Suggestions 50

6.3.2. Facility Upgrade Suggestions 52

APPENDICES

A. FURTHER ACKNOWLEDGMENTS 53

B. VACUUM CHAMBER OPERATION 55

C. VEECO® RF PLASMA SOURCE OPERATION 62

D. MY ADVICE TO A BEGINNING RESEARCHER 66

REFERENCES 70

VITA 73

LIST OF ILLUSTRATIONS

Figure Page

1.1. Eugene Cernan with spacesuit covered with lunar dust. 2

3.1. Photograph taken from inside the vacuum chamber while the Veeco® RF plasma source is in operation. 10

3.2. Schematic and photograph of the vacuum facility. 12

3.3. Oil temperature, vacuum pressure, and cooling water temperature vs. time during the operation of Pump 4. 13

4.1. Measurement locations thus far. 17

4.2. I-V trace with knee at plasma potential and the three regimes labeled. 18

4.3. Photograph of the Langmuir probe rake installed in the vacuum chamber. 20

4.4. Langmuir probe circuit. 21

4.5. Data collected from a voltage sweep taken in this work. 21

4.6. I-V trace with a line fit to the ion saturation regime to estimate ion current through the entire trace. 23

4.7. Polynomial fit of the electron current in the electron saturation and electron retarding regimes, along with the associated residual plot. 23

4.8. Natural log of electron current vs. probe bias with electron temperature and plasma potential lines overlain. 24

4.9. Faraday probe circuit. 29

4.10. Faraday probe as installed in the vacuum chamber. 30

4.11. Determination of electron repelling voltage. 31

4.12. Performance maps of the Veeco® RF ion source, taken at the centerline 17.5" downstream of the exit plane. 34

4.13. Plasma potential plotted against electron temperature. 35

4.14. Spatially resolved plume maps for the Veeco® RF plasma source operating at 500 V, 400 mA. 36

5.1. Geometry for neutrals escaping a single aperture. 39

5.2. Neutral density due to unionized feed gas within the plume. 41

5.3. Neutral density breakdown at an axial distance of 50.16 cm with 20 sccm argon feed and a 400 mA beam with discharge chamber wall temperature of 500 K assumed. 43

5.4. The control volume in question. 43

5.5. Charge exchange ion density as a fraction of total ion density with the source operating at 500 V, 400 mA. 48

5.6. Test article size limit for 20% CEX ions vs. control inputs. 48

6.1. Demonstration of utilizing differential charging to generate power. 50

LIST OF TABLES

Table Page

3.1. Operational envelope of the Veeco® RF plasma source..... 11

3.2. Steady-state pressure for various operating conditions in μTorr. 14

3.3. Mole fraction of argon in the tank. 14

4.1. A comparison between calculated and directly measured floating potential. 22

4.2. Plasma properties attained from the shown I-V trace..... 25

4.3. Comparison between ion flux predictions from Langmuir probe data and that directly measured by the Faraday probe..... 32

1. INTRODUCTION

1.1. MOTIVATION

According to the current administration's space exploration directive, the United States will

> "Lead an innovative program of exploration ... to enable human expansion across the solar system and to bring back to Earth new knowledge and opportunities. Beginning with missions beyond low-Earth Orbit, the United States will lead the return of humans to the Moon for long-term exploration and utilization," [1].

NASA's schedule to accomplish these goals puts humans on the surface of the Moon by 2024, with the end goal being sustainable human presence [2]. Unlike the Apollo missions, these will require prolonged human presence on the surface of the Moon. As such, hazards that were inconvenient for Apollo, but could be worked around, will be crippling for the planned landings. These need to be characterized and protected against as soon as possible. The assessment of these risks are complicated by the fact that the planned missions will take place at the polar regions of the Moon, unlike the Apollo missions where the landings were always in well-lit regions. At the poles, locations of constant darkness and constant light are commonly in very close proximity, leading to two additional major contributors to the risk of such a mission: dust transport, and arcing.

Figure 1.1. Eugene Cernan with spacesuit covered with lunar dust.

1.2. DUST TRANSPORT

Figure 1.1 shows Apollo astronaut Eugene Cernan covered in dust following a lunar excursion. This was taken during Apollo 17 where the mission took place in well-lit regions, where dust transport is expected to be less significant. The upcoming landings, however, will take place at the south pole. The polar regions are continuously at or near the lunar terminator, which is the transition between the light and dark hemispheres.

Dust collection at the lunar terminator is much more significant because of differential surface charging. In a sunlit region, the lunar surface is exposed to phenomena that drive the charge positive: solar wind ion collection, photoelectron emission, and secondary electron emission. These phenomena compete with the collection of solar wind electrons, which occurs very readily due to their very high thermal velocity. With the positive drivers present, a charge equilibrium is attained easily at a low positive potential relative to the ambient [3, 4]. In regions shaded by obstacles, these easily available, positive driving counter-balances are not present. Solar wind electrons have very little problem flowing around an obstacle because of their high mobility. Ions, on the other hand, are much heavier, and are only driven into the wake region by the negative charge caused by the electrons that are already there. The ions' relatively slow response to the obstacle, coupled with

the total unavailability of photo-electron emission due to lack of sunlight, make reaching a charge equilibrium much more difficult [5]. In this situation there are three options to shed negative charge. The first is to create an electric field strong enough to force ions to be collected. The required field strength for this to overcome Debye shielding is unrealistically large [5]. Another option is increased secondary electron emission, but such emission requires an incident electron and is further limited by electron temperature and surface properties [6], so it cannot fully balance the current. The final easy method to shed negative charge is dust grain lofting [5]. Eventually, at a strong enough negative surface potential, the electrostatic repelling forces between like charges will overcome gravitational attraction, resulting in dust particles leaving the surface. The current of negatively charged dust leaving the surface becomes a necessary mechanism to create a charge balance on the lunar surface.

A recent simulation of dust lofting by Orger et. al. [7] found that depending on dust grain size and plasma conditions, the height that dust particles can loft to can be hundreds of meters. This presents a major problem for equipment on the lunar surface. When the dust falls back to the surface it can cover solar panels, abrade sensitive materials, or obstruct moving parts. All of these factors would limit the useful lifetime of rovers, spacesuits, or habitats if unprotected.

1.3. ARCING

A more immediate threat is arcing induced by differential charging. When mobile equipment or an astronaut travels from a region in front of an obstacle to the strongly negative environment behind the obstacle, they bring their charge with them. This creates an especially strong voltage gradient which can lead to arcing. The same is true in reverse when moving from behind the obstacle into a sunlit region. In recent experimental work by Chou [8], it was found that the presence of dust on equipment or spacesuits exacerbates the arcing risk because they introduce a second material with different dielectric properties.

Similar triple junction interfaces, between plasma and two unlike materials, have been observed to cause arcing in spacecraft charging studies. Chou's [8] experiment did not involve the transition between a region exposed to unperturbed plasma and a region behind an obstacle; this means that such transitions are not the only locations where arcing can occur if a dusty environment is involved. Reducing dust contamination, or finding shielding techniques that work despite the presence of dust is paramount for safe long-term lunar missions.

1.4. OBJECTIVES

Considering the immediacy of NASA's plan to return humans to the Moon, there is great need for scientific research on these topics. The main goal of this work is to conduct the first step in pertinent experimental investigations. That is, to answer the following question: Can the Gas and Plasma Dynamics Lab (GPDL) mimic this environment in the Space Tank vacuum facility at Missouri S&T? To this end, the document herein is organized as follows: Section 2 is a literature review, and acts as an overview of the technical challenges involved in creating an environment analogous to solar wind. Section 3 provides an overview of the testing facility and the plasma source used in this work. Section 4 discusses, in explicit detail, the plasma diagnostic probes utilized to measure important properties of the plasma generated within the facility. Section 5 develops a model that utilizes data from a single diagnostic probe taken from a location of interest within the plasma plume to approximate the relative size of the charge exchange (CEX) ion population. This represents a key difference between solar wind and the plasma generated in a vacuum chamber. Finally, Section 6 draws conclusions for this work and suggests a few experimental investigations which the GPDL is capable of at the conclusion of this work. It also discusses inexpensive actions the GPDL could take in the near future to improve its capabilities long-term.

2. LITERATURE REVIEW

2.1. THE LUNAR PLASMA ENVIRONMENT

Solar wind is mostly comprised of mesothermal hydrogen plasma, meaning that its bulk drifting velocity is between the ion's and electron's thermal velocities. For an average solar wind condition, the number density of the plasma is 8.7 cm^{-3}, and the electron temperature is 12 eV. The drifting velocity of solar wind plasma is 4.68 $\times 10^7$cm/s which, for hydrogen, corresponds to an ion energy of 1,144 eV [9]. Electron temperature and plasma density are important because they are used in the calculation of the Debye length, a characteristic length that parameterizes how far electrostatic perturbations can extend into the plasma. Ion energy is important because it determines how readily an ion will be attracted to or repelled from a charged surface.

The plasma environment on the Moon is not constant; depending on its location on its orbit and the solar output at a given moment, these properties can deviate significantly from their aformentioned values. On it's orbit the Moon can be exposed to three types of plasma: unperturbed solar wind, Earth's magnetosheath, and Earth's magnetotail [3]. The Moon spends most of its time in unperturbed solar wind or the magnetosheath, but the time spent in Earth's magnetotail accounts for ~6 days of its evolution around the Earth [3]. In this region it is assumed than the flow is practically stagnant because there is no angular dependence of plasma properties observed by the Lunar Prospector satellite [4]. The environment in Earth's magnetotail is also characterized by very low densities but very high temperatures of 0.016 cm^{-3} and 161 eV, respectively [4].

The plasma environment the lunar surface interacts with is also dependent on variations in solar output. Solar energetic particle events, coronal mass ejections, and geomagnetic storms all perturb this environment. In the data utilized by Orger et al. [7] the

plasma density varied from less than 1 to ~60 cm^{-3}, bulk velocity varied from ~3.8 $\times 10^7$ to ~8 $\times 10^7$ cm/s, and Debye length varied from ~2 to ~30 m. Given this wide variation shown by just a single study, the need for a plasma source with a highly variable output is established.

2.2. THE VACUUM CHAMBER PLASMA ENVIRONMENT

The plasma environment created in a vacuum chamber is fundamentally different than the solar wind environments the GPDL is aiming to recreate. The first, and most easily accounted for difference is that in this work argon plasma is used, instead of hydrogen. Argon is 40 times heavier than hydrogen, so its motion will be much less effected by local electric fields. This is compensated for by matching the kinetic energy of solar wind. This is because whether a charged particle is collected or repelled by a charged surface is determined by its ability to overcome electrostatic forces across the distance of the sheath; thus energy, not momentum, is the pertinent property.

Another easily accounted for difference is that a plasma source will create a plasma much denser than solar wind, thus the vacuum chamber environment needs to be scaled to the lunar environment. The metric with which to do this is the Debye length, λ_D. This is the characteristic length of how far electrostatic perturbations propagate into the surrounding plasma. The sheath thickness, d, is a multiple of the Debye length determined by the surface potential and the Mach number of the plasma entering the sheath, Equations (2.1) through (2.3) (If the plasma is traveling sub-sonic, it accelerates to M=1 at the edge of the sheath). To ensure the sheath thickness around the test article is representative of what will occur on the Moon, the Debye length must be scaled to the same proportion of the test article scale.

$$d = \lambda_D \left[\frac{4\sqrt{2}}{9} \left(\frac{e(\phi_{plasma} - \phi_{surface})}{kT_e} \right)^{3/2} \frac{1}{M} \right]^{1/2} \tag{2.1}$$

where d is the sheath thickness,$\lambda_m athrm D$ is the Debye length, e is the fundamental charge, k is the Boltzmann constant, T_e is the electron temperature, M is the plasma Mach Number, and ϕ_plasma and ϕ_surface are the plasma potential and surface potential, respectively.

$$\lambda_\mathrm{D} = \sqrt{\frac{\varepsilon_0 T_\mathrm{e}}{en}} \tag{2.2}$$

where ε_0 is the permittivity of free space and n is the plasma number density.

$$M = \frac{v_\mathrm{bulk}}{\sqrt{\frac{kT_\mathrm{e}}{m_\mathrm{i}}}} \tag{2.3}$$

where m_i is the mass of an ion and v_bulk is the plasma's bulk drifting velocity.

The last major environmental difference addressed in this work is the presence of low energy ions, which is not significant near the lunar surface. These low energy ions are generated by charge exchange (CEX) collisions with neutrals from either the background gas or unionized feed gas (referred to as CEX ions herein). The presence of CEX ions is a significant issue because, as shown in Equation 2.1, the sheath thickness is dependent on the ion's speed. The CEX ions will create a much thicker sheath, which will impact surface charging. The electric propulsion community has developed a workaround for the presence of unnatural CEX ions in the plume of an ion thruster. Put simply, this method is to take plasma diagnostic data at several different background pressures and extrapolate the results to zero pressure [10, 11, 12, 13]. This method is sound and conceptually simple, but unfortunately it will not work for this study, at least not completely. It is a good way to characterize the difference between a plasma source operating in a vacuum chamber and one operating in space, but it does not account for the difference between plasma generated by an artificial source and real solar wind. Specifically, it does not account for the CEX ions generated by unionized feed (appropriate for its intended application, but not for this work). Polansky [3] also mitigated them using a biased plate to remove them from the

environment. Suggestions for adapting these methods to the GPDL's setup are made in Section 6.3. Currently, the best option for the GPDL is to minimize the CEX ion population by minimizing the background pressure and maximizing the ionization fraction.

3. TESTING FACILITY OVERVIEW AND CHARACTERIZATION

3.1. GENERAL OVERVIEW

This Section provides an overview of the plasma source and vacuum facility used. The benefits of a plasma source with a wide variety of operating conditions is discussed. The operation of the vacuum facility is qualitatively discussed. An experiment to characterize its performance is analyzed. The pressures in the GPDL facility at various flow rates indicate that this facility has similar capabilities to other large scale vacuum facilities in academia. The composition of the background gas is determined, which will be useful when characterizing the population of CEX ions in Section 5.

3.2. VEECO® RF PLASMA SOURCE OVERVIEW

The plasma source utilized in this work was purchased commercially from Veeco® Instruments Inc. This plasma source was chosen because it will readily ionize hydrogen gas, which is a factor of key importance if the chemical interaction between various materials and solar wind is to be investigated. This is a possible direction the GPDL will take long-term. However, in this and in near-future work, argon will be used because it is chemically inert and easier to ionize. This will still allow for several important experimental investigations to be conducted. These include the impact of local topography on lunar surface charging, dust grain lofting in lunar or large asteroid regolith, or coupling between solar wind and planetary magnetic fields. Further potential avenues for near-future work will be discussed in Section 6.3.

The plasma source uses triple-coiled radio frequency (RF) antenna to generate plasma within its discharge chamber. The plasma beam is extracted and focused using three Molybdenum grids: a positively biased screen grid to maintain the plasma discharge

and to drive the beam voltage, a negatively biased accelerator grid to extract ions from the discharge chamber and to aid in beam focusing, and a grounded deceleration grid to focus the beam and to protect the acceleration grid from CEX ion impingement [14]. The plasma source also uses an RF generated neutralizer to produce electrons so that the source does not accumulate a charge during operation. Figure 3.1 shows the source while in operation with a sample test article to show how the GPDL can study the interaction between the plasma plume and an object.

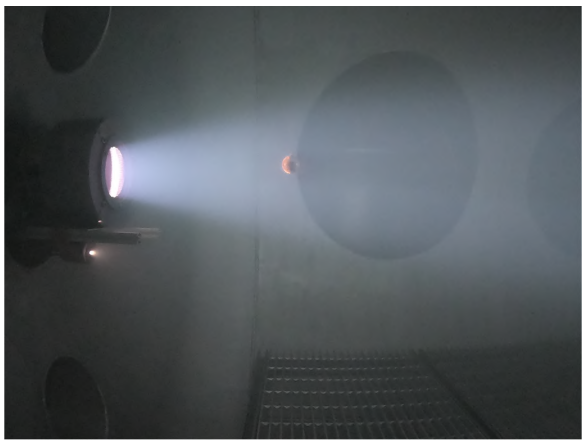

Figure 3.1. Photograph taken from inside the vacuum chamber while the Veeco® RF plasma source is in operation.

The Veeco® source also has a broad operational envelope capable of producing a plasma beam with voltage and current ranging from 100-1500 V and 100-500 mA respectively. Table 3.1 shows 16 points within the envelope for which stability of the beam, defined by a steady discharge and low accelerator impingement current, has already been established [15]. Discharge voltage, discharge current, and accelerator voltage represent the 3 main controller inputs. For a more detailed characterization of the source's performance refer to Sections 4 and 5.

Table 3.1. Operational envelope of the Veeco® RF plasma source.

Discharge Voltage, V	Discharge Current, mA	Accelerator Voltage, V	Accelerator Current, mA	Netralizer Emission, mA	Chamber Pressure, μTorr
100	100	-300	4	125	83.3
100	150	-400	6	188	85.2
100	200	-500	8	250	89.5
250	100	-200	4	125	85.0
250	300	-500	11	375	91.6
250	400	-700	14	500	92.2
500	200	-100	7	250	No Data
500	300	-200	10	376	92.2
500	400	-400	14	500	112.0
1000	200	-100	4	250	96.0
1000	300	-100	6	377	95.3
1000	400	-100	8	500	101.0
1500	200	-300	4	249	98.9
1500	300	-200	6	378	100.0
1500	400	-200	7	500	98.3
1500	500	-200	11	625	108.0

3.3. VACUUM FACILITY OVERVIEW

The vacuum facility utilized in this, and in ongoing work, is cylindrical, 6 feet in diameter, 10 feet in length. The vacuum is pumped by four hot-oil diffusion pumps backed by a rotary vane pump and roots blower. Each diffusion pump operates at a rate of 200,000 L/s if acting on air. Figure 3.2 shows the chamber's setup and dimensions. Because each pump behaves slightly differently depending on which and how many pumps are used, the chamber's base pressure varies in the range 1-3$\times 10^{-5}$ Torr. The vacuum system is set up such that any of the four diffusion pumps can be operated independantly, all four at once, or in any arbitrary combination. Pumps 2 and 3 are the most stable, achieving a true steady state during operation. Pumps 1 and 4, on the other hand, run into thermal issues. Pump 1 will overheat its oil, while Pump 4 rapidly overheats its cooling water. Both can be operated safely, but require regular monitoring such that they may be shut down momentarily to cool when they approach overheating. Diffusion pumps operate based on the existence

of a strong enough oil temperature gradient that convection occurs; as long as a sufficient gradient is present, the pump will continue to produce vacuum whether or not the heating element is on at a given moment. This is displayed empirically by Figure 3.3, a plot of oil and cooling water temperature along with the corresponding tank pressure from when Pump 4 was run on its own. The slight uptick in pressure just after 16:00 corresponds to the incipience of argon gas being fed into the tank, not a variation in pumping performance. Also of note is the spike just before 14:00. This corresponds to the transition between rough and high vacuum. The pressure gauges used in this chamber were designed for atmosphere down to rough vacuum ($\approx 10^{-3}$ Torr) and high vacuum (below $\approx 10^{-5}$ Torr); they do not handle pressures between those two regimes well. The spike is not apparent when the chamber is re-pressurized because that process is much faster; the time in transition is not long enough to appear on the pressure plot [15].

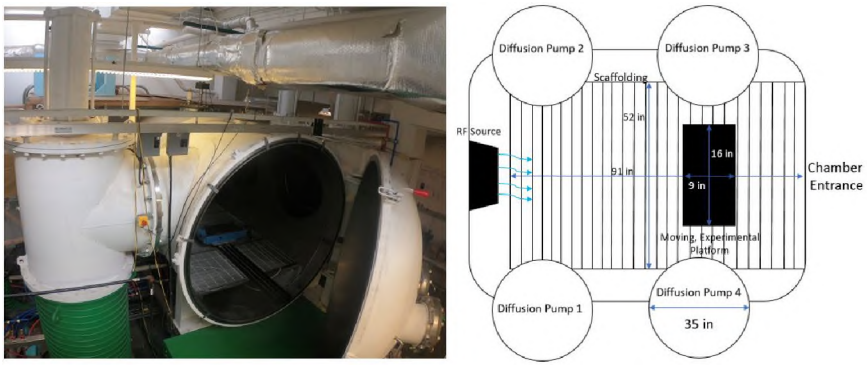

Figure 3.2. Schematic and photograph of the vacuum facility.

3.4. VACUUM CHAMBER CHARACTERIZATION

3.4.1. Experimental Overview. The primary goal of this experiment is to characterize the background gas within the vacuum chamber for gas flow rates which are used during the plasma source's operation. The desired results are tank pressure and composition so collisions with the background gas may be characterized in Section 5.

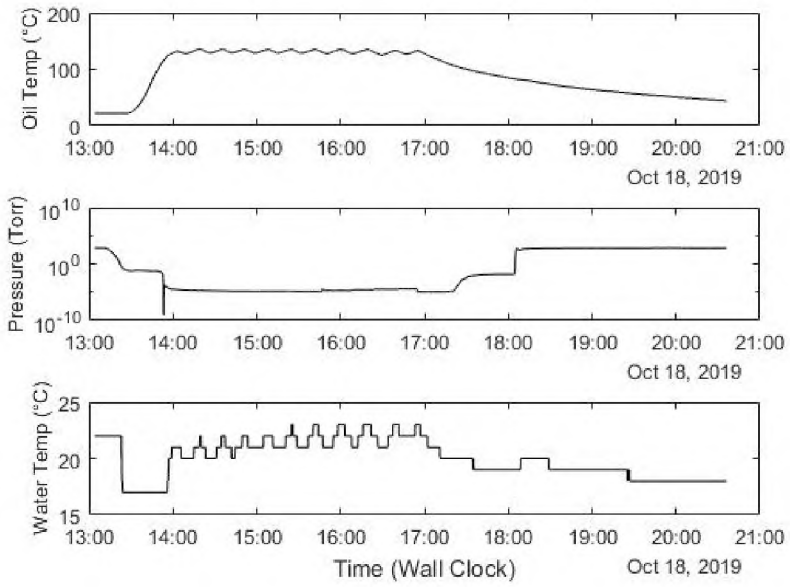

Figure 3.3. Oil temperature, vacuum pressure, and cooling water temperature vs. time during the operation of Pump 4.

Due to cooling system constraints, not every pumping configuration is considered in the performance characterization. Pumps 1 and 4 were not run on their own in the experiment; if only one is needed, Pumps 2 and 3 are better options. Also, all four pumps were not turned on at once. This could be done safely in the future, but it would require constant monitoring instead of regularly checking the oil and water temperatures so it is unlikely to be of value. For each considered pumping configuration, the base pressure for air is determined, after which argon gas is fed into the chamber with flow rates increasing in increments of 10 sccm.

3.4.2. Results and Discussion. Table 3.2 shows the steady-state pressure corrected for argon for each set of operating conditions. For conditions where argon is present these values are corrected according to Equation 3.1 [10].

$$P_{\text{corrected}} = (P_{\text{indicated}} - P_{\text{base}}) \times f_{\text{corr}} + P_{\text{base}} \tag{3.1}$$

where f_{corr} is a correction factor provided by the manual for the pressure gauge [16]; for argon it is 0.8.

Table 3.3 shows the mole fraction of argon in the vacuum chamber. This is done assuming that the presence of nitrogen and oxygen remain relatively constant as more argon is added. This will over-predict their contribution to the background gas composition because nitrogen and oxygen are lighter than argon, therefore, the diffusion pumps will act on them relatively more effectively. Knowledge of the background gas's composition is useful when characterizing the CEX ion population, the presence of which is a notable difference between plasma generated in a vacuum chamber and the solar wind environment. The uncertainty of the indicated pressure is ±30%. The uncertainty of the flow rate is ±0.8% of the reading ±0.1 sccm.

Table 3.2. Steady-state pressure for various operating conditions in μTorr.

Pump Configuration	2	3	2-3	1-2-3	2-3-4
0 sccm argon in (Base Pressure)	30	10	17	14	14
10 sccm argon in	46	32	28	21	21
20 sccm argon in	68	52	37	29	29
30 sccm argon in	95	79	44	34	34
40 sccm argon in	110	100	55	40	40

Table 3.3. Mole fraction of argon in the tank.

Pump Configuration	2	3	2-3	1-2-3	2-3-4
0 sccm argon in (Base Pressure)	0.0	0.0	0.0	0.0	0.0
10 sccm argon in	0.4	0.7	0.4	0.3	0.3
20 sccm argon in	0.6	0.8	0.6	0.5	0.5
30 sccm argon in	0.7	0.9	0.6	0.6	0.6
40 sccm argon in	0.7	0.9	0.7	0.6	0.7

20 sccm argon is the highest flow rate that Veeco® deems necessary to operate this plasma source and is the flow rate which is used hereinafter [14]. At this flow rate the tank settles to pressures between 2.859 and 6.820 $\times 10^{-5}$ Torr. Despite the system's

modest base pressure, the plasma source can be operated at similar background pressures to those within other highly regarded facilities performing similar work [10, 17, 18, 19]. The operating pressures stated therein are slightly lower than those which are attainable by this facility, but the setup herein uses significantly more gas; this vacuum facility's capabilities are comparable. This is due to the very rapid throughput of the diffusion pumps utilized by the GPDL.

4. PLASMA DIAGNOSTICS

4.1. OUTLINE

This Section covers the plasma diagnostics used in this work and provides local plume properties for a sample location vs. controller inputs. Probe theory is well established in literature, but all-encompassing guides to analyzing probe data are hard to come by. This Section aims to fill that gap for Langmuir and Faraday probes by not only stating the methods used, but explicitly showing how each step was performed. Figure 4.1 shows the locations from which data was taken in this work.

Sections 4.2 and 4.3 provide guides to analyze data recorded from their respective probes, including explicit samples and rigorous uncertainty quantification. Section 4.4 shows an example of how different diagnostic probes can be used to validate one-another, known as cross-calibration. Performance maps of plasma property vs. controller inputs are provided and results of an ongoing spatially resolved plume characterization are shown in Section 4.4.

4.2. LANGMUIR PROBES

4.2.1. Overview. Langmuir Probes are a very important tool in plasma diagnostics, as they can be used to measure a number of different properties. This is important because several other plasma probes measure a single property, and Langmuir probes can be used to tie the information from multiple probes together. This is referred to as cross-calibration. In this work, a Langmuir probe is used to find plasma potential, ion and electron density, and electron temperature. Plasma potential and ion density are used to predict ion flux, which is compared to that directly measured by the Faraday probe.

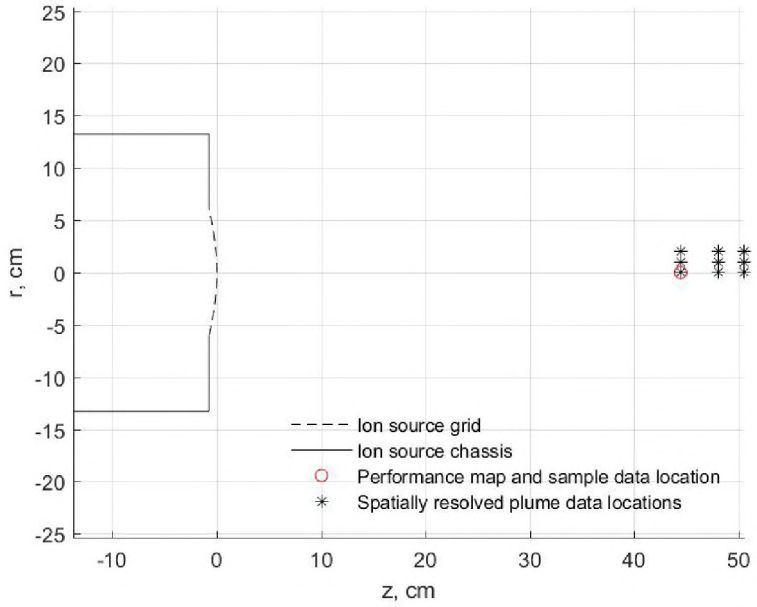

Figure 4.1. Measurement locations thus far.

Langmuir probes are simply a biased electrode immersed in plasma. The applied bias is swept from ion saturation, sufficiently negative to repel all electrons, to electron saturation, sufficiently positive to repel all ions. Typically this means a small to moderate (more than 10, less than 100) negative voltage to a moderate positive (more than 30, less than 100) voltage. At sufficiently negative voltages the ion current will usually saturate, and in an ideal probe the electron current will saturate at and above the plasma potential. True electron current saturation is rare for a multitude of reasons. The most significant of cause is that the plasma sheath surrounding the probe expands with increasing voltage, allowing more electrons to be attracted to the probe. Instead of a maximum collected current, electron saturation typically appears as a 'knee' in the current vs. voltage characteristic (I-V trace herein). This is shown in Figure 4.2.

The I-V trace is split into three regimes, ion saturation, electron retarding, and electron repelling. The ion saturation regime is voltages below the X intercept. The X intercept is known as the floating voltage, and is where equal number of electrons and ions are col-

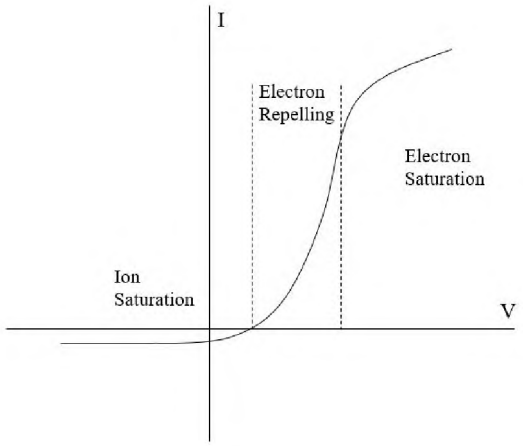

Figure 4.2. I-V trace with knee at plasma potential and the three regimes labeled. The axes are arbitrary.

lected by the probe. The current collected in the ion saturation region is mostly, and at sufficiently negative voltages (where the current plateaus), all ions. The electron retarding region is between the floating potential and plasma potential. This regime selectively filters electrons according to their energy; near the floating potential, only the high energy tail of the electron's energy distribution can make it to the probe without being repelled; as the plasma potential is approached, the number of electrons that can overcome the energy barrier to be collected increases. In this regime ions are still being attracted; the ion current collected by the probe is relatively unchanged [12, 20]. The current is positive in the electron retarding regime because electrons have much less mass and are therefore much more mobile; they are more readily available to be collected. The electron saturation regime is voltages above the plasma potential. Here, the probe attracts electrons and repels ions. In stationary plasma, at voltages above the plasma potential no ions are collected. In a moving plasma, this is only true for surfaces parallel to the motion of the plasma. To repel ions from being collected by non-parallel surfaces, the applied voltage must be greater than the ion's retarding voltage, at voltages this high the attracted electron current would likely melt the probe [21]. This additional ion current stays relatively constant throughout

the I-V trace, so it shifts the entire trace negative by a small constant. The largest impact of this is that it causes the over-prediction of ion density. This can be accounted for in post-processing, but methods to do so presuppose knowledge of the direction of the ion's local bulk motion[21, 22]. Luckily, for a cylindrical probe, if the length of the probe is sufficiently greater than the radius the impact of this end-effect is negligible [22].

The Langmuir probes used in this work are cylindrical, with diameter 1.65 and length 20.5 mm. Voltage is applied by B& K Precision© and BlackJack Test Ins.™ power supplies. Current is measured via the voltage drop across a 14.97 kΩ shunt resistor, read by two Tektronix® V2221 voltage probes. One of the probes directly measured the probe bias, the other measured the voltage at the other side of the shunt, V_{Power} in Figure 4.4. Data was recorded synchronously with a DATAQ® DI-145, removing the need for an automatic sweep (other than for convenience). The probes were placed on a rake, shown in Figure 4.3, to interrogate multiple plume locations in quick succession. All voltage sweeps were taken from -30 to 60 V. The probe circuit is shown in Figure 4.4.

4.2.2. RF Compensation. Usually, for RF generated plasma, the plume is perturbed by the propagating RF signal; this results in plasma potential fluctuating at the RF frequency with a magnitude of T_e/e [23]. This perturbs the I-V trace such that useful information cannot be obtained. RF compensated probes, which essentially act as narrow-pass filters tuned to the RF frequency, are often required to obtain meaningful data from an I-V trace. However, comparison of our (uncompensated) collected data to that in Lobbia and Beal [21] from a Hall Effect thruster, where breathing and spoke modes cause similar plasma fluctuations to an RF signal, shows that RF noise is not significant in our setup. In the published data the magnitude of the noise increases substantially in the electron saturation region (above the plasma potential) [21]. The noise magnitude in our data is constant throughout the trace, and on the order of the voltage probe uncertainty divided by the shunt's resistance. Therefor the experimental noise is more likely characterized by measurement inaccuracy than by fluctuating plasma properties.

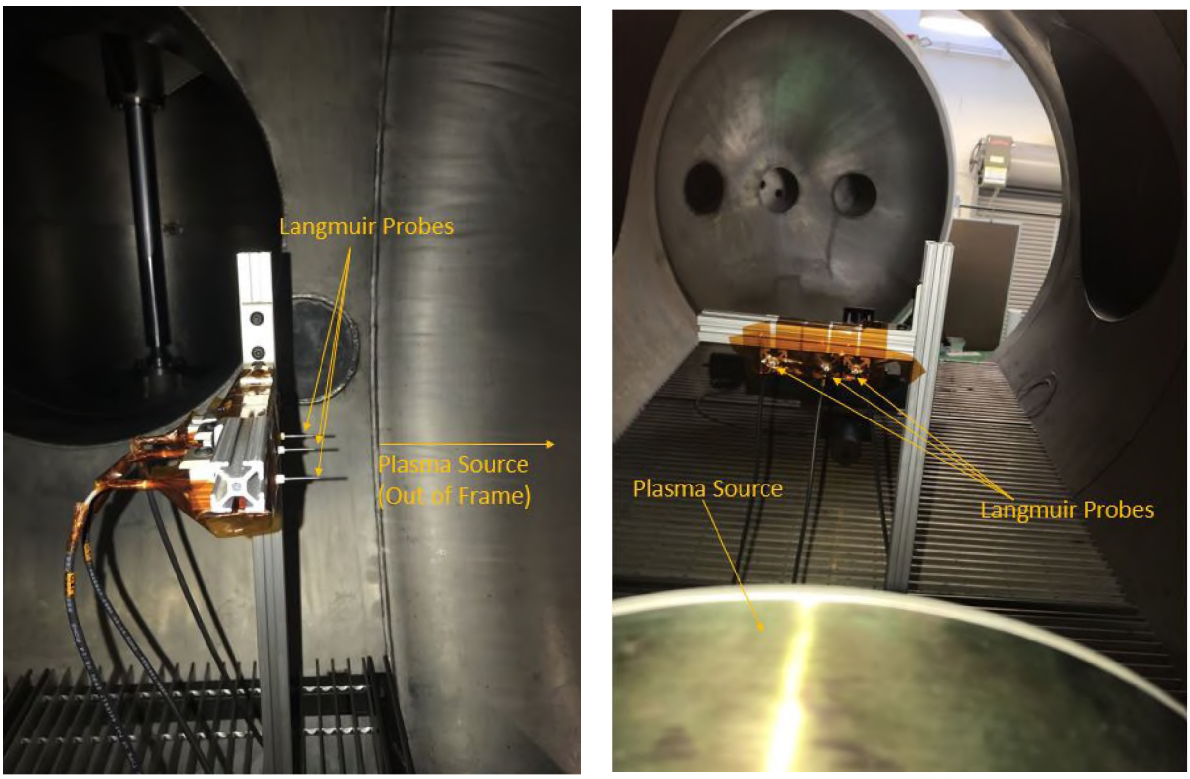

(a) Side View (b) Front View

Figure 4.3. Photograph of the Langmuir probe rake installed in the vacuum chamber.

4.2.3. Data Analysis. Consider the I-V trace shown in Figure 4.5 taken at the centerline of the plume, 17.5" downstream of the exit plane. For this trace the source was outputting a 400 mA beam at 500 V. The Accelerator grid was biased to -400 V. There is no 'knee' at the plasma potential, because the electron Debye length is on the same order as the probe radius; above the plasma potential the sheath expands too rapidly for a change in slope of the I-V trace to be apparent. This claim will be verified at the end of this assessment.

The first step in analyzing Langmuir probe data is to find the floating potential [12, 20, 21, 24]. Unfortunately root finding algorithms fail for this data set, even those that bracket the root. This is because in the ion saturation regime the signal to noise ratio is poor; any conventional root finding algorithm has many false zeros to converge to. Instead,

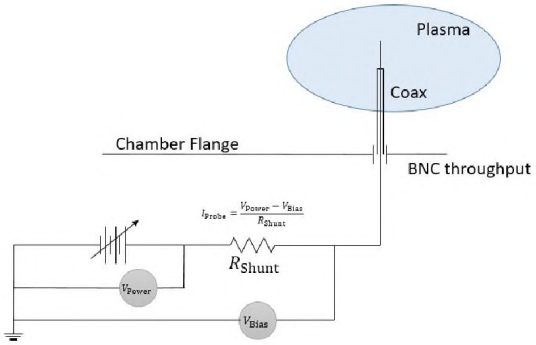

Figure 4.4. Langmuir probe circuit.

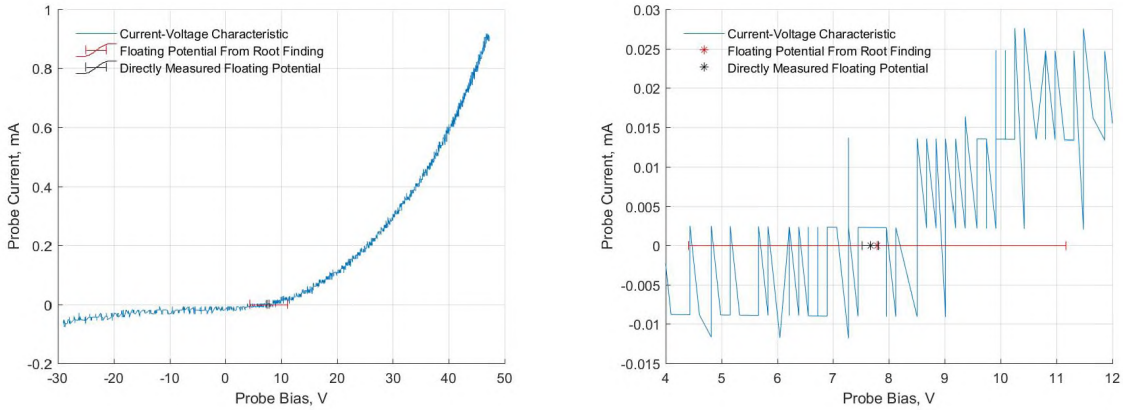

(a) The whole probe characteristic

(b) Zoomed in on the floating potential

Figure 4.5. Data collected from a voltage sweep taken in this work.

the floating potential was found by starting at the highest probe bias and approximating the current by averaging together the data inside a window with half-width equal the voltage probe's uncertainty. The considered voltage is iteratively decreased until the returned average is within the noise threshold of the data. This approach is unorthodox, so it was validated by measuring the floating potential directly. This was done by unplugging the probe from the power circuit and measuring the voltage it maintained. Of course, the voltage probe circuit has a very large, but finite, resistance to ground. However, the floating voltage is small, so the amount the resulting measurement will be perturbed from the true floating potential is negligible. The floating potential found by the root of the I-V trace and by direct measurement are in agreement to within the uncertainty of the voltage probe's

Table 4.1. A comparison between calculated and directly measured floating potential.

	From the I-V Trace	Directly Measured
Value, V	7.7888	7.6706
Uncertainty, V	3.3786	0.1520
Current to Ground, mA	N/A	0.0022

measurement. This is shown in both Table 4.1 and Figure 4.5, see Section 4.2.5 for details for uncertainty quantification. The associated current to ground was calculated using the most conservative estimate of the voltage probe's effective resistance to ground: 3.5 MΩ. The resulting current to ground is approximately one fifth of the magnitude of the noise, determined by inspection of Figure 4.5b. Thus, the algorithm to find the root of the I-V trace is to be trusted, and direct measurement of floating potential is unneeded and therefor will not be performed hereinafter. It should also be noted that the directly measured floating potential will not be used in the determination of plasma properties, it was simply a verification that the algorithm converges to the physical value.

With the floating potential found, the next step is to remove the ion current from the I-V trace. This is done by fitting a line through the ion saturation regime, as shown in Figure 4.6 [21]. It is worth noting that the line is fit through only the truly linear portion of the ion saturation regime, not the entire voltage range. This line is then used to approximate ion current throughout the trace. Subtracting the ion current yields the isolated electron current. A semi-log plot of the electron current for voltages above the floating potential is needed to find electron temperature and plasma potential. The natural logarithm operation inflates the impact of the data's noise, so a 4^{th} order polynomial is fit to the electron current above the floating potential. The fit and residuals are shown in Figure 4.7. For the sample shown R^2 is 0.9993, so the fit accurately represents the data and plotting the natural logarithm of the data fit will return meaningful results.

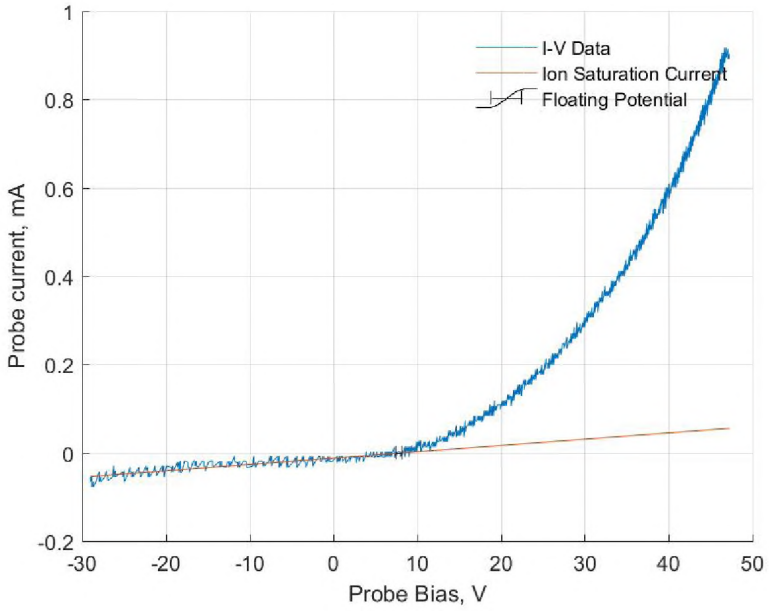

Figure 4.6. I-V trace with a line fit to the ion saturation regime to estimate ion current through the entire trace.

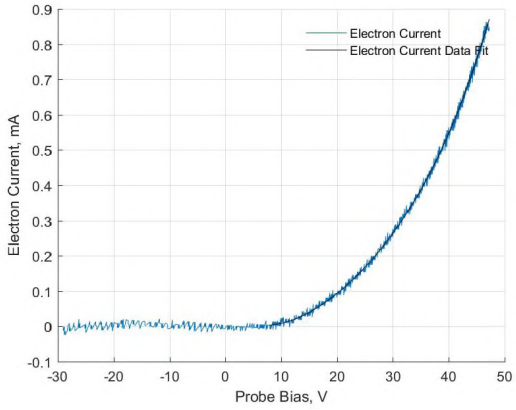

(a) The fourth order polynomial fit overlain onto the raw data.

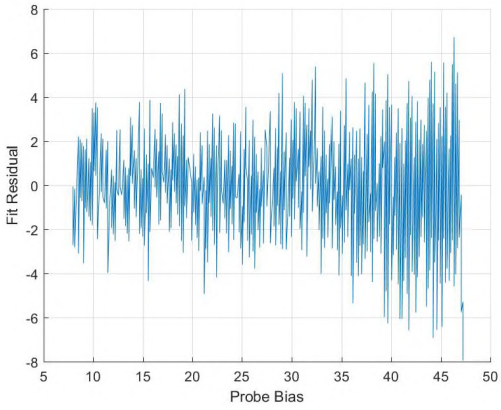

(b) Residual plot, as a percentage of the average electron current.

Figure 4.7. Polynomial fit of the electron current in the electron saturation and electron retarding regimes, along with the associated residual plot.

On the semi-log plot, a line is fit to the first few voltages above the floating potential, referred to as the electron temperature line. Electron Temperature is the inverse slope of this line. Often, a small, shallow sloped tail exists just above the floating potential, which will artificially increase the measured electron temperature. This tail is algorithmically ignored by instead defining the electron temperature line as a tangent line through the point of maximum slope. A second line, referred to as the plasma potential line, is drawn through the last few data points in the log plot. The voltage where these two lines intersect is the plasma potential. The log plot of electron current and overlain electron temperature and plasma potential lines is shown in Figure 4.8.

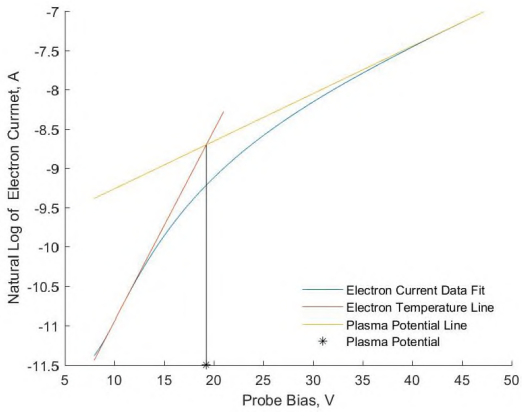

Figure 4.8. Natural log of electron current vs. probe bias with electron temperature and plasma potential lines overlain.

Electron and Ion density are then found using equations (4.1) and (4.2).

$$n_e = \frac{I_{e,sat}}{eA_{probe}}\sqrt{\frac{2\pi m_e}{eT_e}} \tag{4.1}$$

$$n_i = \frac{\exp(1/2)I_{i,sat}}{eA_{sheath}}\sqrt{\frac{m_i}{eT_e}} \tag{4.2}$$

Table 4.2. Plasma properties attained from the shown I-V trace.

Property	Value		Uncertainty, same units as property
T_e, eV	4.128		0.8663
ϕ_{plasma}, V	19.2526		0.152
n_e, cm^{-3}	1.718×10^7		4.384×10^6
n_i, cm^{-3}	8.647×10^8		7.129×10^8
$\lambda_{D,i}$, cm ($r_{probe}/\lambda_{D,i}$)	0.0514	(1.6061)	6.018×10^{-4}
$\lambda_{D,e}$, cm ($r_{probe}/\lambda_{D,e}$)	0.3644	(0.2264)	2.185×10^{-4}

where $I_{e,sat}$ is the electron current collected at the plasma potential, and $I_{i,sat}$ is the ion current collected at a strongly negative bias relative to the plasma potential. Because the linear fit of ion saturation assumed a thin sheath, it is appropriate to assume $A_{sheath} \approx A_{probe}$. Finally, the electron and ion Debye lengths are found using Equations (4.3) and (4.4).

$$\lambda_{D,e} = \sqrt{\frac{\varepsilon_0 T_e}{e n_e}} \tag{4.3}$$

$$\lambda_{D,i} = \sqrt{\frac{\varepsilon_0 T_e}{e n_i}} \tag{4.4}$$

The results of this assessment are shown in Table 4.2. The Debye length for electrons is just less than one fourth of the probes radius, this is why the sheath expands so rapidly above the plasma potential and methods that rely on finding the 'knee' in the unaltered I-V trace are not reliable for finding the plasma potential for this setup.

4.2.4. Accounting for Sheath Expansion. According to Lobbia and Beal [21], for this Debye length scale the results need to be corrected for orbital motion limited effects. That is, including angular momentum considerations in the calculation of ion density [21]. Nominally, the electron current does not need correcting because it is measured from data collected at the plasma potential, where no sheath exists. In this work, accounting for sheath expansion is neglected for two reasons, one from literature and one from experimental result: Polansky [3] used similar methods for conditions where the Debye length is

much longer relative to probe radius and attained valid results, and more importantly, that predictions of ion flux made from the measured plasma potential and ion density agree with the ion flux directly measured by the Faraday probe. See Section 4.4 for details.

4.2.5. Uncertainty. With plasma diagnostics, it is important to report uncertainty, because the measurement error between setups can be vastly different. Equations (4.5) through (4.11), adapted from Lobbia and Beal [21] and Lobbia and Gallimore [25] achieve this. For the probe setup therein, discreet voltage sweeps were utilized, with current vs. voltage measurements taken a few volts apart. The separation between measurements is denoted as ΔV_{bias} in the equations below. This work utilized a continuous sweep, hence using the difference between voltages in the sweep would result in a singularity. As a rough workaround, this work used the span of the voltage range for which the electron temperature line is a good fit in the semi-log electron current plot, defined by the range in voltages where the difference between the line and the semi-log plot is less than 0.3%. Quantitative justification for this substitution is difficult, but qualitatively the resulting trend is reasonable, if a wider portion of the data fits into the linear region of the semi-log plot the uncertainty in the electron temperature will decrease. Making this substitution doesn't change the equation in an appreciable way, it simply uses an alterative value to normalize the probe bias uncertainty to. Anecdotally, this substitution returns a value on the same order as the difference between voltages in Lobbia and Gallimore [25].

$$\partial A_{\text{probe}} = 2\pi\sqrt{\left(L_{\text{probe}} + r_{\text{probe}}\right)^2 \partial r_{\text{probe}}^2 + r_{\text{probe}}^2 \partial L_{\text{probe}}^2} \tag{4.5}$$

$$\partial I_{\text{probe}} = 2I_{\text{probe}}\sqrt{\left(\frac{\partial V_{\text{bias}}}{I_{\text{probe}} R_{\text{shunt}}}\right)^2 + \left(\frac{\partial R_{\text{shunt}}}{R_{\text{shunt}}}\right)^2} \tag{4.6}$$

$$\partial T_{\text{e}} = T_{\text{e}}\sqrt{2\left(\frac{\partial V_{\text{bias}}}{\Delta V_{\text{bias}}}\right)^2 + 2\left(\frac{\partial I_{\text{e,sat}}}{I_{\text{e,sat}}} \cdot \frac{T_{\text{e}}}{\Delta V_{\text{bias}}}\right)^2} \tag{4.7}$$

$$\partial n_e = n_e \sqrt{\left(\frac{\partial I_{e,sat}}{I_{e,sat}}\right)^2 + \left(\frac{\partial A_{probe}}{A_{probe}}\right)^2 + \left(\frac{\partial T_e}{2T_e}\right)^2} \tag{4.8}$$

$$\partial n_i = n_i \sqrt{\left(\frac{\partial I_{i,sat}}{I_{i,sat}}\right)^2 + \left(\frac{\partial A_{probe}}{A_{probe}}\right)^2 + \left(\frac{\partial T_e}{2T_e}\right)^2} \tag{4.9}$$

$$\partial V_p = \sqrt{(\partial V_{bias})^2 + (\Delta V_{bias})^2} \tag{4.10}$$

$$\partial V_f = \sqrt{(\partial V_{bias})^2 + \left(T_e \frac{\partial I_{i,sat}}{I_{i,sat}}\right)^2} \tag{4.11}$$

where, in this case, the operator ∂ means uncertainty. Uncertainty in Debye length is not explicitly defined in Lobbia and Beal [21] or Lobbia and Gallimore [25] , but its value can be easily determined using the same standard propagation techniques, Equations (4.12)-(4.13).

$$\partial \lambda_{D,e} = \lambda_{D,e} \sqrt{\left(\frac{\partial T_e}{2T_e}\right)^2 + \left(\frac{\partial n_e}{2n_e}\right)^2} \tag{4.12}$$

$$\partial \lambda_{D,i} = \lambda_{D,i} \sqrt{\left(\frac{\partial T_e}{2T_e}\right)^2 + \left(\frac{\partial n_i}{2n_i}\right)^2} \tag{4.13}$$

4.3. FARADAY PROBE

Similar to a Langmuir probe, Faraday probes are simply an electrode immersed in plasma with a voltage bias applied and current measured via a voltage drop across a shunt resistor. What is special to a Faraday probe are all of the design considerations that specialize it to measuring ion current density. Instead of the collecting surface being a narrow cylinder it is a flat circle with a relatively large radius surrounded by a guard ring. Nominally, a constant negative voltage will be applied that is sufficiently strong enough to repel

all electrons from reaching the collecting surface, i.e. at or below the electron repelling voltage. The resulting collected current is divided by the collection area yielding the ion current density. This process is shown by Equations (4.14) and (4.15). The negative in (4.15) is to account for collected ion current being considered negative by the sign conventions used in this work. The guard ring is biased to the same voltage as the collector; its purpose is to mitigate edge effects by creating a uniform sheath across the surface of the collector, effectively shielding the collector from perturbations caused by the corner of the collecting surface [3, 11, 12].

$$I_{\text{probe}} = \frac{V_{\text{power}} - V_{\text{bias}}}{R_{\text{shunt}}} \tag{4.14}$$

$$j_{\text{ion}} = \frac{-I_{\text{probe}}}{A_{\text{collector}}} \tag{4.15}$$

Faraday probes are a very powerful tool in plasma diagnostics. They can be translated across the plume to measure the radial distribution of the ion flux from which the plume divergence half-angle can be attained. The variance of the ion flux distribution with background pressure is of great importance in the electric propulsion community; this is because it represents a key facility effect that needs to be accounted for when predicting the actual in-orbit performance of gridded ion and Hall-effect thrusters [10, 11, 13]. Due to hardware and time constraints this is not performed in this work, but is planned for in the very near future. In this work, Faraday probe data is only taken along the centerline of the plume at the location indicated by the red circle in Figure 4.1 to act as a validation of Langmuir probe data. This is obviously not ideal, but the information lost is not a debilitating factor because this work focuses on locally mimicking the lunar plasma environment, not characterizing the performance of a thruster. Brown et al. [11] recommends that when a Faraday probe is to be swept across the plume a cylindrical coordinate system be used in the near field and a spherical coordinate system be used in the far-field. For

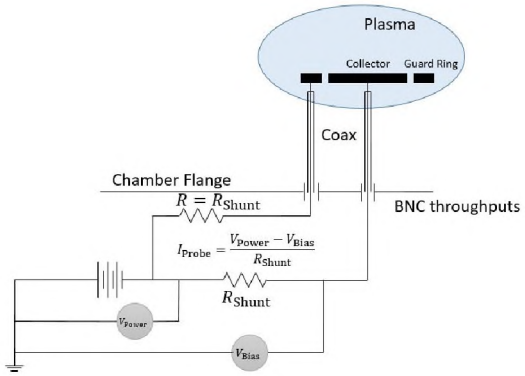

Figure 4.9. Faraday probe circuit.

the near field it is also recommended that the probe's collecting surface stay parallel to the source's exit plane and for the far field the probe stay pointed at the centerpoint of the exit [11]. Following these coordinate systems and pointing conventions will simplify the application of geometric correction factors according to the methods therein. These corrections are neglected in this work because all measurements were taken along the centerline. For both near and far field, the spatial resolution of the probe is the diameter of the collector; measurements taken within that distance of each-other cannot be considered unique.

The Faraday probe circuit used in this work is shown in Figure 4.9. The probe's mounting within the vacuum chamber is shown in Figure 4.10. In this work an additional shunt resistor of equal value was used between the guard ring and power supply in an attempt to keep it at the same bias as the collector.

Nominally, the electron repelling voltage is known beforehand and the probe can simply be biased to that value to measure ion flux. This value cannot be arbitrarily assumed, however, and if it is unknown it must be found by sweeping to probe voltage until the current stops measurably increasing. This typically occurs at small to moderate negative voltages, but in some instances it is below -100 V [11]. The electron repelling voltage at the centerline for a given axial distance can be assumed sufficiently negative to repel electrons for every measurement at that axial distance [11] (or sweep radius if in the far

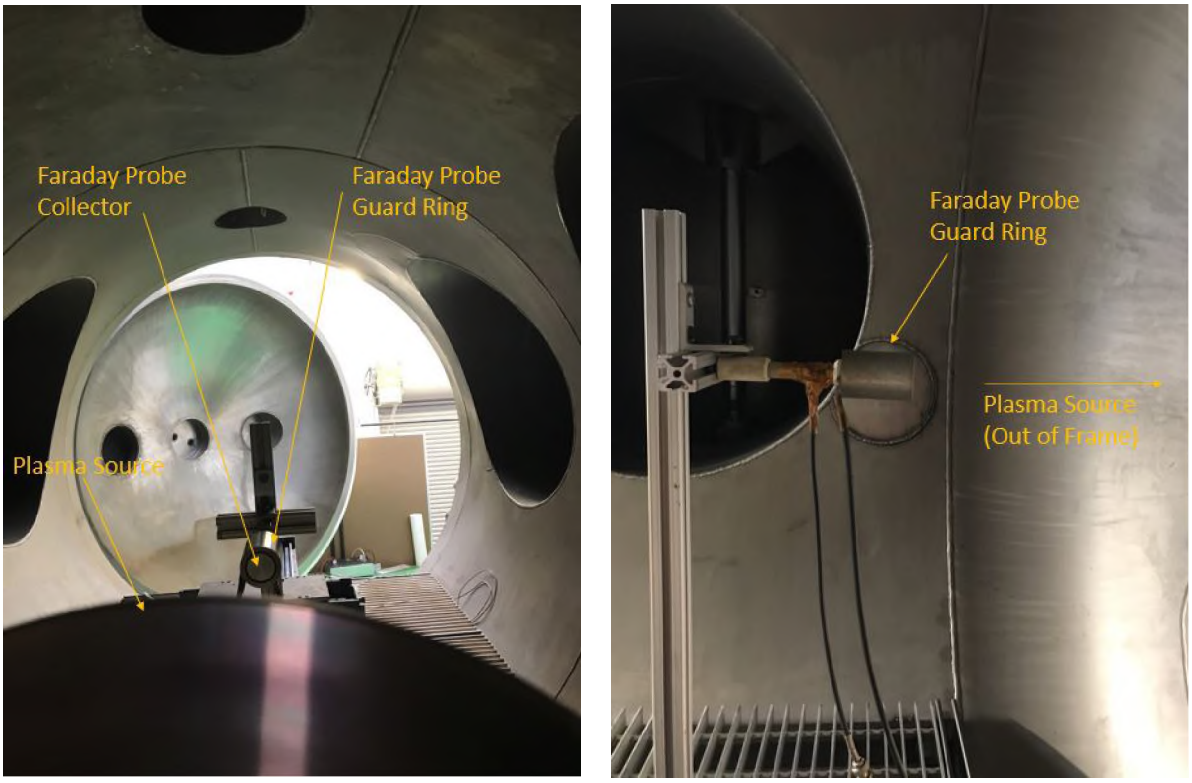

(a) Front view (b) Side view

Figure 4.10. Faraday probe as installed in the vacuum chamber.

field). The results for such a sweep are shown in Figure 4.11a. This voltage sweep asymptotically approaches a value then begins increasing again. Current saturation is assessed using the analytic model for electron flux to a charged surface, Equation (4.16) and Figure 4.11b. The collected current saturates before the anomalous current increase begins so the anomaly isn't a significant issue. The cause of this increasing current is still unknown, but a reasonable explanation is that the sheath begins expanding beyond what the guard ring can protect against at very negative voltages. The uncertainty of the measured ion flux is defined using standard uncertainty propagation practices, Equation (4.17).

$$j_e = en_e\sqrt{\frac{T_e}{2\pi m_e}}\exp\left(\frac{e(V_{bias}-\phi_{plasma})}{kT_e}\right) \tag{4.16}$$

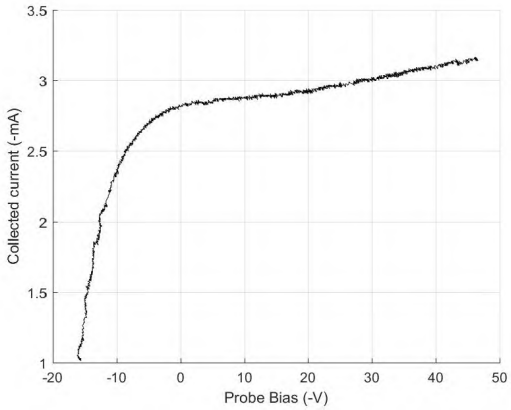

(a) Sweep to find the electron repelling voltage

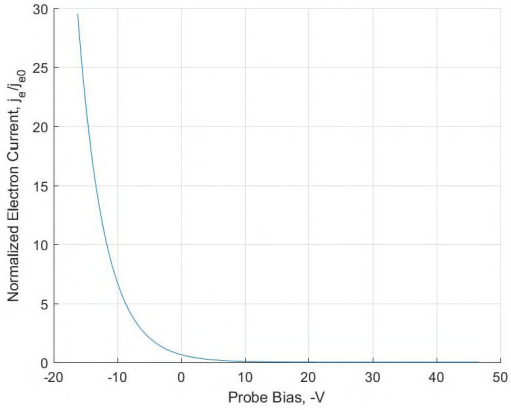

(b) Normalized electron flux from the analytic model

Figure 4.11. Determination of electron repelling voltage.

where j_e is the electron current density to a surface with voltage V_{bias} immersed in plasma with potential ϕ_{plasma}.

$$\partial j_{ion} = \sqrt{\left(\frac{\partial I_{probe}}{I_{probe}}\right)^2 + 2\left(\frac{\partial d_{collector}}{d_{collector}}\right)^2} \tag{4.17}$$

4.4. RESULTS

4.4.1. Local Plume Properties. Table 4.3 compares the ion current density predicted from Langmuir probe data, calculated from Equations (4.18)-(4.19), with that directly measured from the Faraday probe.

$$j_{ion,predicted} = en_i v_i = en_i \sqrt{\frac{2e}{m_i}(V_{beam} - \phi_{plasma})} \tag{4.18}$$

$$\partial j_{ion,predicted} = j_{ion,predicted} \sqrt{\left(\frac{\partial n_i}{n_i}\right)^2 + \frac{1}{2}\left(\frac{\partial \phi_{plasma}}{\phi_{plasma}}\right)^2} \tag{4.19}$$

In 14 of the 16 data points the difference is less than uncertainty, and in 12 of the data points the difference is less than half of the uncertainty. The mean discrepancy normalized to the uncertainty is 34.49%.

Table 4.3. Comparison between ion flux predictions from Langmuir probe data and that directly measured by the Faraday probe.

Beam Voltage, V	Beam Current, mA	Ion current density, $mAcm^{-2}$ Predicted (Langmuir)			Measured (Faraday)			Difference/ Uncertainty
100	100	0.1733	±	0.2717	0.0886	±	0.0047	0.3117
100	150	0.1661	±	0.2223	0.1293	±	0.0048	0.1655
100	200	0.1684	±	0.2916	0.1617	±	0.0049	0.0230
250	100	0.1254	±	0.6227	0.1348	±	0.0048	-0.0151
250	300	0.7015	±	0.7129	0.3558	±	0.0059	0.4849
250	400	0.3264	±	0.455	0.4758	±	0.0067	-0.3283
500	200	0.7634	±	0.4993	0.3139	±	0.0056	0.9002
500	300	0.6845	±	0.6084	0.4504	±	0.0065	0.3848
500	400	0.5003	±	0.5414	0.5681	±	0.0074	-0.1193
1000	200	0.7744	±	0.6004	0.3435	±	0.0058	0.7177
1000	300	0.5853	±	0.618	0.4651	±	0.0066	0.1945
1000	400	0.7217	±	0.5937	0.4889	±	0.0068	0.3921
1500	200	0.4902	±	0.7527	0.3111	±	0.0056	0.2379
1500	300	1.2664	±	0.7567	0.3712	±	0.006	1.1830
1500	400	1.3273	±	0.8356	1.4464	±	0.0066	-0.1425
1500	500	2.5744	±	1.7679	0.578	±	0.0077	1.1292
							mean	0.3449

Polansky [3] used ion flux measured by the Faraday probe along with plasma potential to determine the ion density, reducing uncertainty. In this work, due to both time and hardware constraints, Faraday probe data is only available at the centerline, 44.45 cm downstream of the exit. Given this limitation, that method is not available for the entire measurement field, so the Faraday is used only to validate the Langmuir probe data for a test case. The uncertainty for predicted ion flux is high, regularly greater than 100%, because uncertainty in ion saturation current, electron temperature, probe area, and plasma potential are all involved in its calculation. Despite the high uncertainty, the difference

between predicted and measured ion flux is the best validation metric available with the given hardware because nearly all of the Langmuir probe's measured properties go into the prediction of ion flux.

With the probe data validated by cross calibration, the Langmuir probe data can be used to create a meaningful performance map of the plasma source. This is shown for each plasma property of interest in Figure 4.12. Not many quantitative conclusions can be drawn from these maps without a specific set of target conditions, but qualitative examination of trends is productive to further verify the probe readings and will help in future work. Many of the trends displayed make physical sense. Floating potential has obvious positive trends with both beam current and beam voltage, because it will take a higher voltage to reach current equilibrium in a more ion-rich environment and with higher energy ions. There is a positive correlation between electron temperature and plasma potential, Figure 4.13. This is to be expected because more energetic electrons force a greater difference between plasma potential and floating potential. With the beam operating at 300 mA the ion density is greater at 300 V than 1000 V, the same total current but moving faster reults in a less dense flow. These maps do not account for the accelerator grid voltage, but each beam current and voltage set has an associated ideal accelerator voltage. This voltage which represents a minimum impingement current; thus accelerator voltage is not a truly independent variable if the ideal voltage is used in all cases [14]. Also of note is that these maps contain no information regarding plume divergence. The expected trend that a higher beam current at the same voltage and lower beam voltage at the same beam current result in denser plasma is followed generally, but not universally because of unaccounted differences in plume divergence.

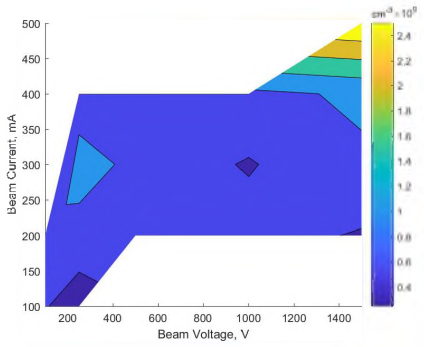

(a) Ion density

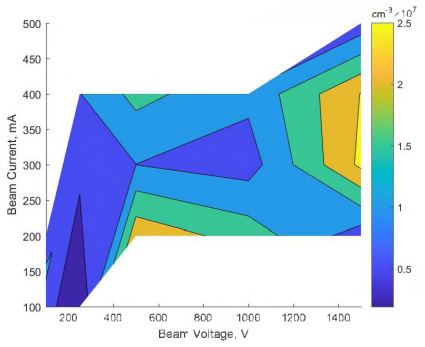

(b) Electron density

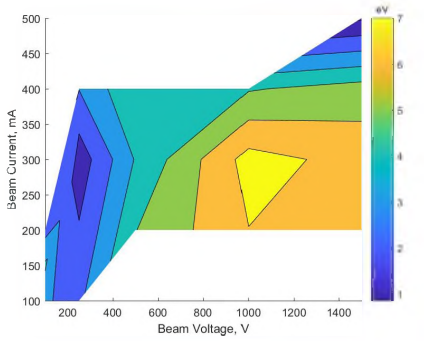

(c) Electron temperature

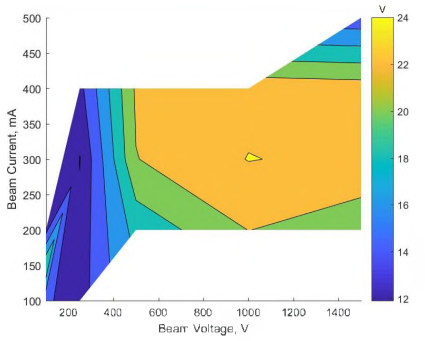

(d) Plasma potential

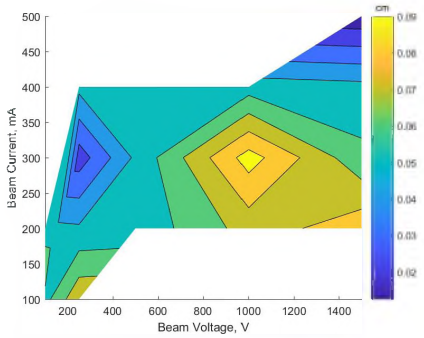

(e) Ion Debye length

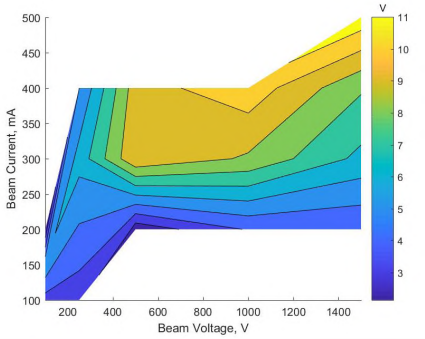

(f) Floating potential

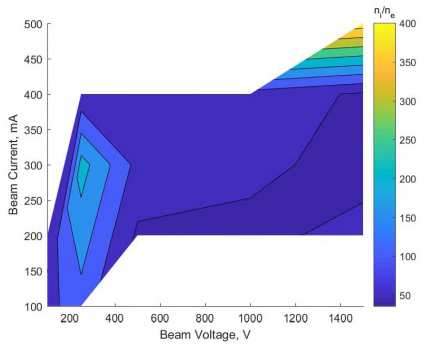

(g) n_i/n_e

Figure 4.12. Performance maps of the Veeco® RF ion source, taken at the centerline 17.5" downstream of the exit plane.

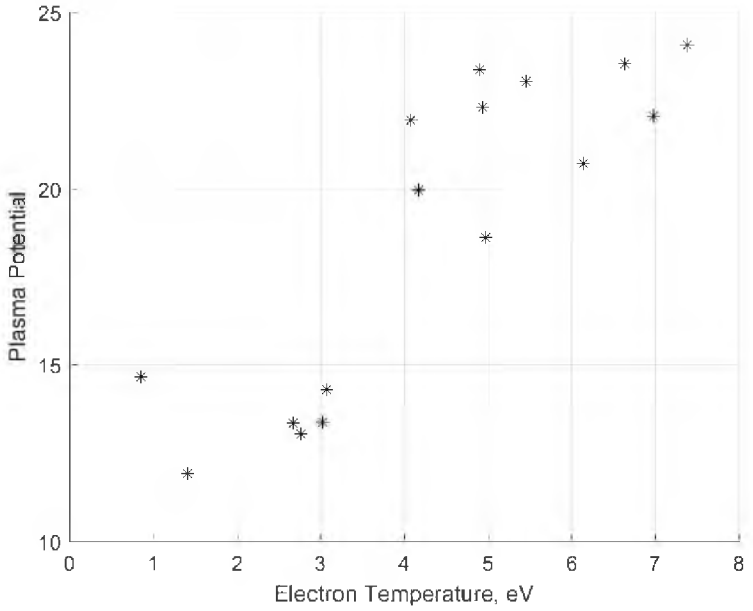

Figure 4.13. Plasma potential plotted against electron temperature.

4.4.2. Ongoing Plume Characterization. Figure 4.14 shows spatially resolved maps of the plasma properties created when the plume is operating at 500 V and 400 mA. This is an ongoing work, as only 9 locations have thus far been considered, but the information provided is sufficient to obtain initial results for the CEX population model proposed in Section 5, which is what everything thus far has been building towards.

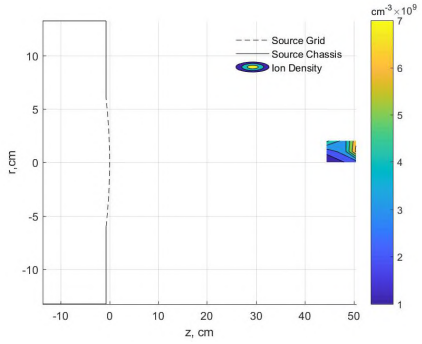

(a) Ion density

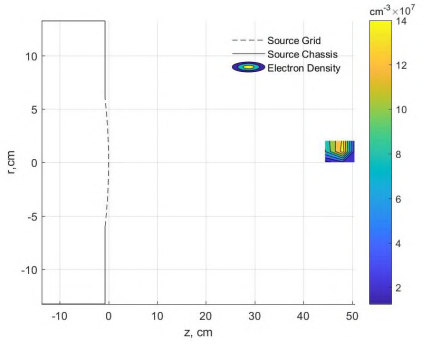

(b) Electron density

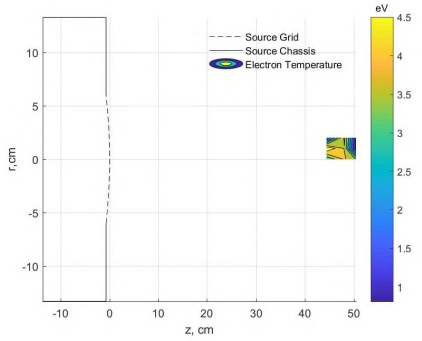

(c) Electron temperature

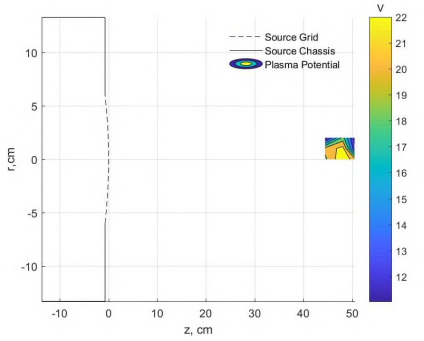

(d) Plasma potential

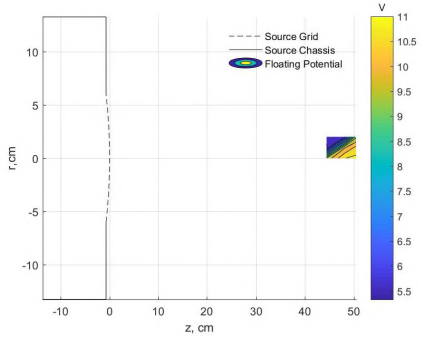

(e) Floating potential

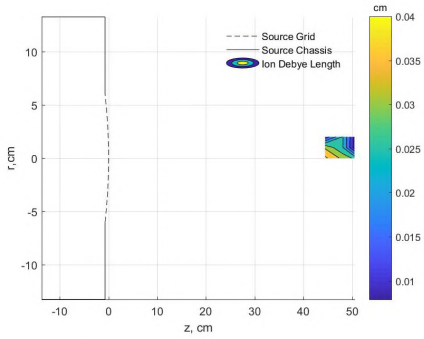

(f) Ion Debye length

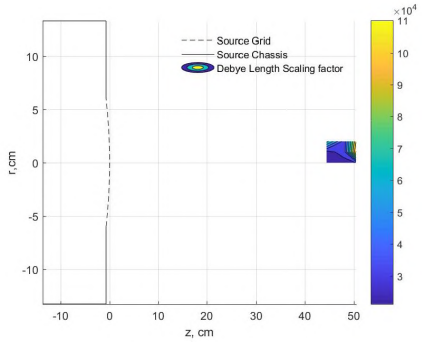

(g) Debye length scaling factor

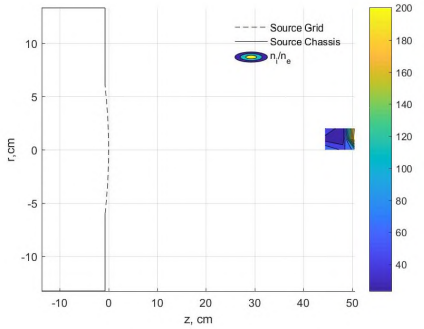

(h) n_i/n_e

Figure 4.14. Spatially resolved plume maps for the Veeco® RF plasma source operating at 500 V, 400 mA.

5. MODELING LOCAL CHARGE EXCHANGE ION DENSITY

5.1. REASONING FOR THE MODEL

Knowledge of the local CEX ion population is a significant gap in the plume characterization methods mentioned thus far. The GPDL initially planned to obtain this using a retarding potential analyzer, RPA. RPA's act similarly to a Faraday probes, but by forcing the ions to flow through a series of electrostatically biased grids they selectively filter ions based on their energy. By sweeping the applied voltage the probe directly measures the ion energy distribution. Nominally, the CEX population would appear as a small bump on the low energy tail of an otherwise Maxwellian distribution. Unfortunately, due to time constraints caused by the campus shutdown in response to COVID-19, the required hardware is still not available for use. The GPDL is working to get this hardware operational, but the time-frame is unknown. With the RPA currently unavailable, an alternative approach to determining the relative CEX ion population size is desired. This Section proposes and applies a model to determine if such an assessment can obtain meaningful results without performing a fully kinetic simulation of the plume as discussed by Wang et al. [26]. It should be noted that this is meant to be a back-of-the-envelope approximation. The simplicity of this model means that it will maintain its value, even after the RPA is working. The translating stage takes approximately 90 minutes to interrogate the plume per probe. Due to current cooling constraints on the plasma source this corresponds to the maximum duration the source can be operated in one day without burning out the recirculating water pump. To perform a full characterization of a new operating condition, it will take a full day of experimentation per probe. This is simply too great a time commitment if a particular set of plume conditions is sought. This is where the usefulness of this model is realized, it only requires Langmuir probe data for an abridged portion of the plume. Such data takes

approximately 15 minutes to obtain, post-process, and assess using this model, allowing for 6 operating conditions to be tested in a single day. Once a set of desired conditions is found, then more rigorous plume characterization methods can be applied.

The layout of the remainder of this Section is as follows: Section 5.2 defines properties of the plume that cannot be directly determined by the current diagnostic probe array. Section 5.3 shows the derivation of a model of local CEX ion density population. Section 5.4 presents a spatially resolved map of the CEX ion density for the plasma source operating at 500 V, 400 mA, and a potential application for which that operating condition would be useful is discussed. A performance map that shows the maximum test article size that would occupy the region where CEX ions account for less than 20% of the total ion density vs. operating conditions is also presented.

5.2. MODEL INPUTS

In order to model the production of low energy CEX ions, there are a few things that need to be known about the local plasma that can't be found with common plasma diagnostics. Namely, those are the local neutral density and the CEX collision cross section. The cross section can be found by Equation (5.1), which returns the value in m^2 [27].

$$\sigma_{CEX} = [k_1 + k_2 \ln(E)]^2 \times 10^{-20} \tag{5.1}$$

where E is the ion energy in eV. For argon, k_1 and k_2 are 5.17 and -0.25, respectively. This model was developed based on a data fit of multiple experiments spanning ~1 - ~10^5 eV, so it is valid for the entire operational envelope of the plasma source used in this work.

In order to model unionized feed gas's contribution to the neutral density within the plume, first consider a single grid aperture to be treated as a point source of neutral particles. The distance, L from the opening and angle from the opening's center-line, α, are defined in Equations (5.2), (5.3), and shown in Figure 5.1 [28].

$$L = \sqrt{r^2 + z^2} \tag{5.2}$$

$$\cos(\alpha) = \frac{z}{L} \tag{5.3}$$

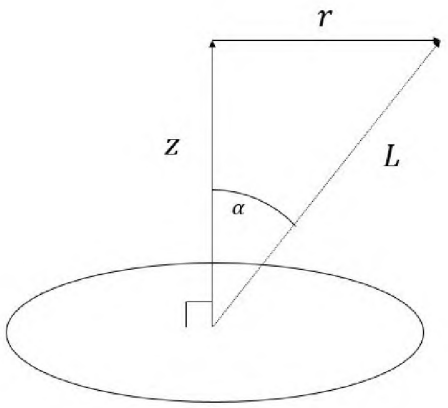

Figure 5.1. Geometry for neutrals escaping a single aperture.

Equations (5.4) and (5.5) provide the angular distibution, T, of particles traveling through the aperture [28].

$$T(\alpha) = 1 - \left\{ \frac{2}{\pi}(1-\kappa) \left| \arcsin\left(\frac{\bar{t}\tan(\alpha)}{2}\right) + \frac{\bar{t}\tan(\alpha)}{2}\sqrt{1-\left(\frac{\bar{t}\tan(\alpha)}{2}\right)^2} \right| \right\} + \frac{4}{3\pi}(1-2\kappa)\frac{1-\left|1-\left(\frac{\bar{t}\tan(\alpha)}{2}\right)^2\right|^{3/2}}{\frac{\bar{t}\tan(\alpha)}{2}} \tag{5.4}$$

if $\alpha \leq \arctan(2/\bar{t})$, or:

$$T(\alpha) = \kappa + \frac{4}{3\pi}\frac{1-2\kappa}{\frac{\bar{t}\tan(\alpha)}{2}} \tag{5.5}$$

if $\alpha > \arctan(2/\bar{t})$. The neutral density downstream of a single grid aperture is given by Equation (5.6) [28].

$$\frac{n(r,z)}{n_0} = F_{\text{scm}}\frac{R^2}{4}T(\alpha)\frac{z}{L^3} \tag{5.6}$$

where F_{scm} is a correction factor that will account for the presence of the screen grid and deceleration grid. To simplify the assessment this is assumed to be unity because their radii are much wider than the accelerating grid [28]. The parameter $\bar{t}$ is the aperture thickness divided by the aperture radius, and κ is defined by Equation (5.7)

$$\kappa = \frac{\sqrt{\bar{t}^2+4}-\bar{t}}{2+\frac{4}{\sqrt{\bar{t}^2+4}}} \tag{5.7}$$

The above set of equations defines a single aperture's contribution to the unionized feed in the plume. For each location the contribution of each aperture must be summed together. Figure 5.2 shows normalized neutral particle density contours for gas escaping through and single aperture and for the total grid. This formulation is also only valid when a grid aperture has a thickness to radius ratio less than 8 and the considered location is far enough downstream that the point source assumption is valid [28]. For this work that threshold is arbitrarily defined to be 20 aperture radii downstream of the grid.

Because Equation (5.6) returns the density normalized to the discharge chamber density, these contours will remain unchanged regardless of the source's operating conditions. To find the actual density, knowledge of the discharge chamber's neutral density is

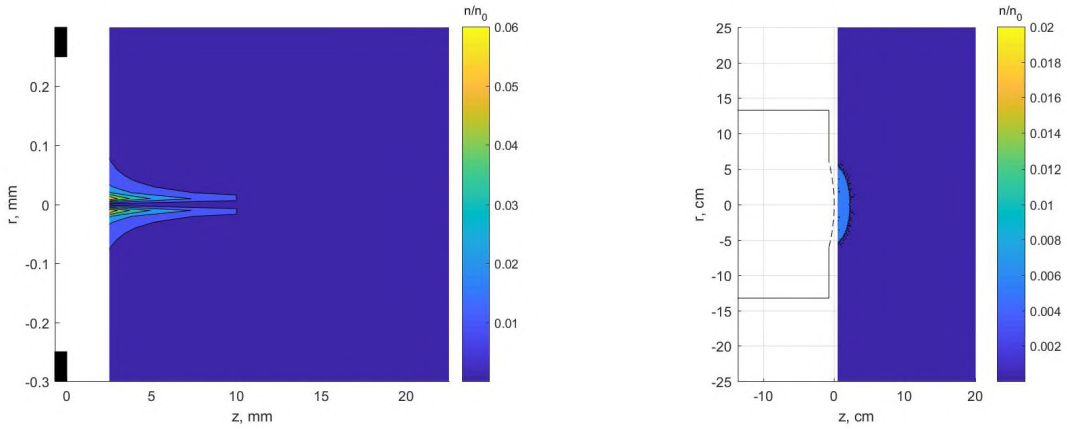

(a) Neutrals escaping a single aperture.

(b) Neutrals in the plume

Figure 5.2. Neutral density due to unionized feed gas within the plume.

required. This can be found using conservation of matter: all of the gas that enters the discharge chamber is either ionized and leaves in the beam or escapes as a neutral. This balance is shown in Equation (5.8).

$$\frac{\dot{m}_{\text{gas,in}}}{m_{\text{n}}} = \frac{I_{\text{beam}}}{e} + \dot{n}_{\text{n,out}} \tag{5.8}$$

where $\dot{m}_{\text{gas,in}}$ is the mass flow rate of feed gas into the ion source, m_{n} is the mass of an individual feed gas molecule, and $\dot{n}_{\text{n,out}}$ is the number flow rate of neutral particles escaping through the grids.

Assuming each grid aperture radius is less than the mean free path within the discharge chamber, and that the neutrals inside the discharge chamber are at stagnated equilibrium, the rate at which neutrals leave the discharge chamber can be defined in terms of a velocity distribution function (VDF) simplified to 1-dimension shown in Equation (5.9)

$$\dot{n}_{\text{n,out}} = A_{\text{escape}} n_0 \int_0^{\infty} v * \left(\frac{m_n}{2\pi kT}\right)^{1/2} \exp\left(-\frac{m_n}{2kT} v^2\right) dv \tag{5.9}$$

The above integral is evaluated, leaving Equation (5.10)

$$\dot{n}_{\mathrm{n,out}} = A_{\mathrm{escape}} n_0 \frac{kT}{m_{\mathrm{n}}} \left(\frac{m_n}{2\pi kT} \right)^{1/2} \tag{5.10}$$

where A_{escape} is the sum of the open grid area. Plugging Equation (5.10) into (5.8) and solving for discharge chamber density yields (5.11):

$$n_0 = \left[\frac{\dot{m}_{\mathrm{gas,in}}}{m_{\mathrm{n}}} - \frac{I_{\mathrm{beam}}}{e} \right] \frac{m_{\mathrm{n}}}{kTA_{\mathrm{escape}}} \left(\frac{2\pi kT}{m_n} \right)^{1/2} \tag{5.11}$$

Unfortunately this requires a temperature, which is unknown. Literature has established that the wall temperature of the discharge chamber serve as a good approximation [23, 28]. Unfortunately the discharge chamber wall temperature is an unknown quantity in our system. Typically in literature it is around 500 K [23, 28, 29]. Exact knowledge of the discharge chamber wall temperature is ideal, but as shown in Figure 5.3, the contribution of unionized feed gas is approximately 2 orders of magnitude less significant than the background gas; thus the sensitivity of the model to the discharge chamber wall temperature will be small. The model for CEX cross section is only valid for symmetric collisions, i.e. collisions with argon, but since argon, accounts for about 80% of the local neutral density, nitrogen and oxygen will be approximated to have the same cross section as argon. Since this approximation is only applied to 20% of the neutral population, the inaccuracy it causes is small relative to other assumptions that go into the CEX model developed in Section 5.3, which will be discussed therein.

5.3. MODEL DERIVATION

Consider a thin annular control volume (CV) concentric with the center-line of the plume, a cross section of which is shown in Figure 5.4. Assume that plasma potential, neutral density, and beam ion density are constant within the control volume. The accumulation of CEX ions within this control volume can be expressed by Equation (5.12).

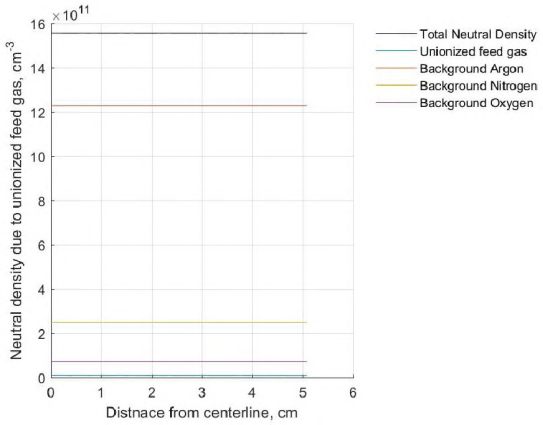

(a) Each species contribution to total neutral density

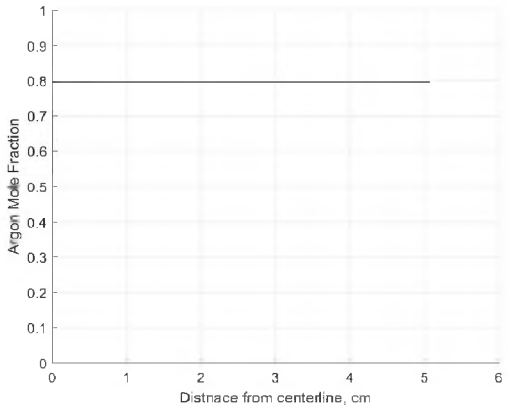

(b) Mole fraction of argon

Figure 5.3. Neutral density breakdown at an axial distance of 50.16 cm with 20 sccm argon feed and a 400 mA beam with discharge chamber wall temperature of 500 K assumed.

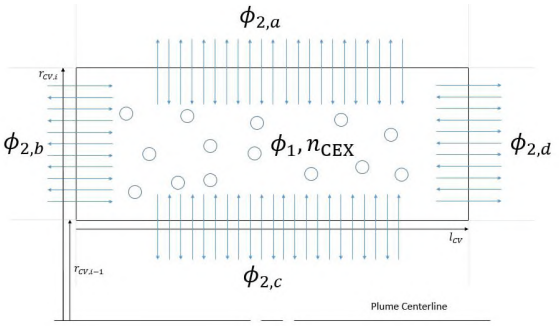

Figure 5.4. The control volume in question.

$$\dot{n}_{\mathrm{accum}} = \dot{n}_{\mathrm{in}} - \dot{n}_{\mathrm{out}} + \dot{n}_{\mathrm{gen}} \tag{5.12}$$

The simplest of the three terms is the generation of CEX ions, defined by Equations (5.13) and (5.14).

$$n_{\mathrm{i,Beam}} = n_{\mathrm{i}} - n_{\mathrm{i,CEX}} \tag{5.13}$$

$$\dot{n}_{\mathrm{CEX,gen}} = \pi r_{\mathrm{cv}}^2 l_{\mathrm{cv}} n_{\mathrm{neu}} n_{\mathrm{i,Beam}} v_{\mathrm{i,Beam}} \sigma_{CEX} \tag{5.14}$$

Flux of CEX ions into and out of the CV is more complex. The governing equations for a single wall of a CV is provided by Equations (5.15) through (5.22). This set of equations needs to be solved for each wall of every CV. This assessment utilizes the Neumann boundary condition, $\nabla\phi_{\mathrm{N}} = \nabla\phi_{\mathrm{N-1}}$ to model the flux of CEX ions out from the domain. This neglects inward flux of CEX ions from the region outside the model's domain. Generally, this will only effect the region upstream of solution domain, because that is nominally the only external region in which local potential gradients will push CEX ions into the solution domain [18, 26, 30]. Thus, the lost information is mitigated by assessing how much the CEX density changes by incrementally including additional upstream planes into the solution. Results will only be reported for areas in which the addition of the final upstream plane changes the local CEX ion density by less than 1%.

The flux of CEX ions across a surface is defined in terms of the VDF for a drifting Maxwellian population, Equation (5.15) shows this, but this method assumes that potential gradients are the only driving force behind drifting motion:

$$\Gamma_{\mathrm{CEX}} = n_{\mathrm{CEX}} \int_0^{\infty} v \left(\frac{m_{\mathrm{i}}}{2\pi kT}\right)^{1/2} \exp\left(-\frac{m_{\mathrm{i}}(v - v_{\mathrm{d}})^2}{2kT}\right) \mathrm{d}v \tag{5.15}$$

where v_{d} is the drifting velocity. For convenience, the integral split into two parts, (5.16):

$$\Gamma_{\mathrm{CEX}} = n_{\mathrm{CEX}} \left(\frac{m_{\mathrm{i}}}{2\pi kT}\right)^{1/2} \left[\int_{v_{\mathrm{d}}}^{\infty} v \exp\left(-\frac{m_{\mathrm{i}}(v - v_{\mathrm{d}})^2}{2kT}\right) \mathrm{d}v + \int_0^{v_{\mathrm{d}}} v \exp\left(-\frac{m_{\mathrm{i}}(v - v_{\mathrm{d}})^2}{2kT}\right) \mathrm{d}v\right] \tag{5.16}$$

For simplicity, the function is shifted by v_d, such that the function is centered at 0, (5.17):

$$\Gamma_{\mathrm{CEX}} = n_{\mathrm{CEX}} \left(\frac{m_{\mathrm{i}}}{2\pi kT}\right)^{1/2} \left[\int_0^{\infty} v \exp\left(-\frac{m_{\mathrm{i}}(v - v_{\mathrm{d}})^2}{2kT}\right) \mathrm{d}v + \int_{-v_{\mathrm{d}}}^{0} v \exp\left(-\frac{m_{\mathrm{i}}(v - v_{\mathrm{d}})^2}{2kT}\right) \mathrm{d}v\right] \tag{5.17}$$

The first integral term becomes the right half of the stationary Maxwellian distribution, which has already been solved in Equation (5.9). The second integral term is found by taking advantage of symmetry about 0, which can then be trivially solved with a substitution, shown in Equation (5.18):

$$\int_{-v_{\mathrm{d}}}^{0} v \exp\left(-\frac{m_{\mathrm{i}} v^2}{2kT}\right) \mathrm{d}v = \int_0^{v_{\mathrm{d}}} v \exp\left(-\frac{m_{\mathrm{i}} v^2}{2kT}\right) \mathrm{d}v = \frac{kT}{m_{\mathrm{i}}} \left[1 - \exp\left(-\frac{m_{\mathrm{i}} v_{\mathrm{d}}^2}{2kT}\right)\right] \tag{5.18}$$

Substituting Equations (5.18) and the result of the non-drifting forward flux into Equation (5.15) yields an expression for CEX ion flux across an arbitrary plane, Equation (5.19):

$$\Gamma_{\mathrm{CEX}} = n_{\mathrm{CEX}} \left(\frac{m_{\mathrm{i}}}{2\pi kT}\right)^{1/2} \frac{kT}{m_{\mathrm{i}}} \left\{1 + \left[1 - \exp\left(-\frac{m_{\mathrm{i}} v_{\mathrm{d}}^2}{2kT}\right)\right]\right\} \tag{5.19}$$

Drifting velocity magnitude is defined by Equation (5.20):

$$v_{\mathrm{d}} = \sqrt{\frac{2e\,|\phi_1 - \phi_2|}{m_{\mathrm{i}}}} \tag{5.20}$$

where ϕ_1 and ϕ_2 are the plasma potential inside and outside the CV, respectively.

From this, the rate at which CEX ions are leaving and entering the CV across a given wall are expressed by Equations (5.21) and (5.22), respectively:

$$\dot{n}_{\mathrm{CEX,out}} = A_{\mathrm{wall}} n_{\mathrm{CEX},1} \left(\frac{m_{\mathrm{i}}}{2\pi kT}\right)^{1/2} \frac{kT}{m_{\mathrm{i}}} \left\{1 + \xi \left[1 - \exp\left(-\frac{e|\phi_1 - \phi_2|)}{kT}\right)\right]\right\} \tag{5.21}$$

$$\dot{n}_{\mathrm{CEX,in}} = A_{\mathrm{wall}} n_{\mathrm{CEX},2} \left(\frac{m_{\mathrm{i}}}{2\pi kT}\right)^{1/2} \frac{kT}{m_{\mathrm{i}}} \left\{1 - \xi \left[1 - \exp\left(-\frac{e|\phi_1 - \phi_2|)}{kT}\right)\right]\right\} \tag{5.22}$$

The subscript 1 refers to the value inside the control volume, and 2 refers to the value outside the control volume, just across the boundary in question. ξ is a correction factor equal to 1 if $\phi_1 > \phi_2$ and -1 if $\phi_1 < \phi_2$. This accounts for the direction that the VDF was shifted to center it about the origin. Expressed mathematically $\xi = \frac{\phi_1 - \phi_2}{|\phi_1 - \phi_2|}$.

The procedure for the assessment is as follows:

1. Divide the probe data into small annular control volumes, interpolating as needed.
2. Consider only the first few downstream-most planes for which data is available.
3. Guess the CEX ion density as 90% of the measured ion density for each control volume considered.
4. Calculate beam ion density and CEX ion generation rate across the solution domain.
5. Calculate diffusion of CEX ions across each wall.
6. Calculate resulting CEX ion accumulation rate for each control volume.
7. Propagate forward a small time-step, updating guess for CEX ion density appropriately.
8. Iterate 4-7 until accumulation is sufficiently small.
9. Add a new plane into the calculation domain, start over at 3.
10. Repeat 9 until the entire domain is resolved, report data for only the areas where adding the final plane results in less than 1% change.

It is worth reiterating that this model is intended to be a computationally inexpensive approximation of CEX ion density in the plume. The model is best utilized as a tool to rule out operating conditions or plume locations that are too laden with CEX ions to

obtain meaningful experimental data; to make a rudimentary estimate to determine if further investigation is warranted. Another use for this model is to approximate the size limit of a test article for which the local CEX ion population is small. Using the local Debye length this will also return the corresponding maximum lunar surface size we can mimic. For this use, the model is still only a rough approximation. If a deterministic profile of the local CEX population size is desired, then either robust fully kinetic simulation or direct measurement with an RPA is needed.

5.4. RESULTS AND DISCUSSION

Figure 5.5 shows the results of this assessment for the beam operating at 500 V and 400 mA. Data is only presented for regions for which the addition of the last upstream axial plane resulted in less than a 1% change in the local CEX ion density. Qualitatively, local maxima in plasma potential correlate to local minima in CEX ion density, which matches expectation. The region in which the ratio of CEX ion density is less than 20% (highlighted in red) is approximately 3.5 cm diameter, which has been arbitrarily chosen to represent the cutoff between a region that reasonably mimics the lunar environment and one that is too laden with CEX ions. From Figure 4.14 the relative scale to the lunar surface is ≈30,000, thus the region of low CEX density corresponds to ~ 1 km on the lunar surface. This is slightly larger than the simulation domain in [9], a recent simulation around a lunar boulder. This operating condition will be most useful in investigations pertaining to the conditions around a similar small structure, such as a boulder or man-made structure. If mimicking such an environment under average solar wind conditions, albeit with lower than normal velocity, is the goal, then a more rigorous characterization of this operating condition is a useful allocation of resources.

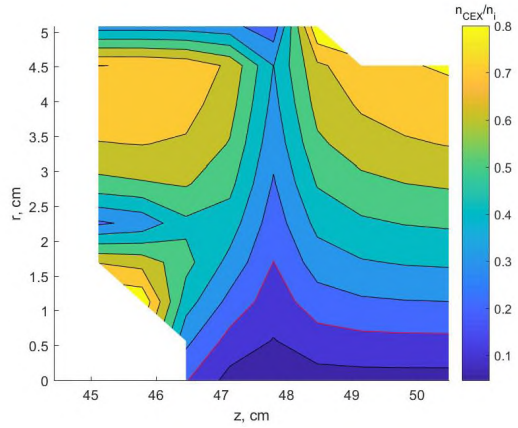

Figure 5.5. Charge exchange ion density as a fraction of total ion density with the source operating at 500 V, 400 mA.

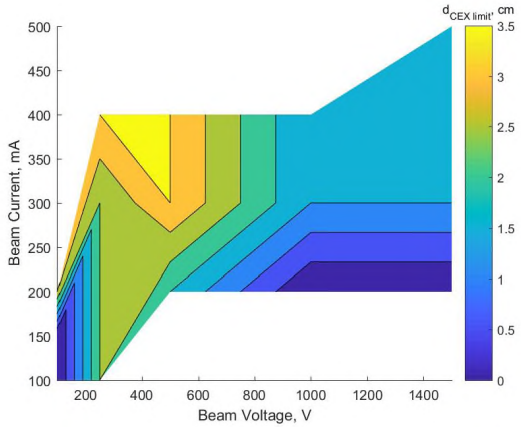

Figure 5.6. Test article size limit for 20% CEX ions vs. control inputs.

Figure 5.6 shows the maximum test article size that can be placed in plume while staying within a region of less than 20% CEX ions. Because solar wind varies in Debye length, Figure 5.6 was not normalized to the lunar surface in order to keep its usefulness as broad as possible.

6. SUMMARY, CONCLUSION, AND RECOMMENDED FUTURE WORK

6.1. SUMMARY

At the completion of this work the GPDL has the tools required to conduct experimental research on the lunar plasma environment. Section 3 shows that the Space Tank vacuum facility can attain similar background pressure during plasma source operation to other facilities doing similar research. The post-processing algorithms described in Section 4 are written as 'black-box' functions which the lab can easily utilize. The CEX ion density model developed in Section 5 is a useful tool that will aid in the search for a set of operating conditions which creates an analog for the desired lunar environment. This method reduces the time required to perform a preliminary plume assessment from days to minutes. The code utilized therein can also be treated as a black box function with a few minor alterations.

6.2. CONCLUSION

This work shows that the facility utilized by the GPDL is capable of meaningfully recreating the lunar plasma environment. The lab's experimental team is ready to begin work that will contribute to the nation's goal of a sustained human presence on the Moon and meaningfully collaborate with the simulation team who is already contributing to the field. The GPDL is left in very capable hands.

6.3. RECOMMENDED FUTURE WORK

6.3.1. Experiment Suggestions. Recently, the GPDL demonstrated an opportunity for *in-situ* resource utilization (ISRU) offered by differential surface charging. Because the surface in front of an obstacle is charge positive and behind the obstacle is charge negative, if the two regions were electronically connected current would flow and power could be extracted. A photograph of this powering an LED and a rough diagram of the setup is shown in Figure 6.1. An approximation of the maximum power available to this system is given by the formulas in Equations 6.1 and 6.2.

(a) Differential surface charging powering an LED.

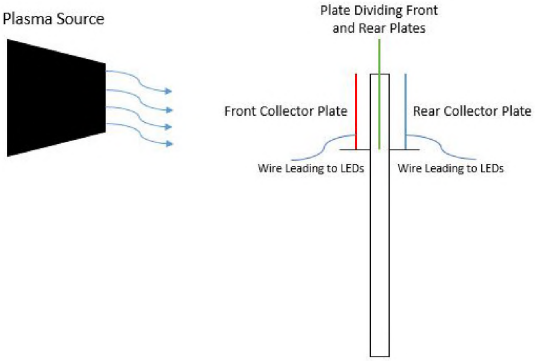

(b) Representative schematic. The front collector plate is exposed to ions and electrons; the rear collector plate is only exposed to electrons.

Figure 6.1. Demonstration of utilizing differential charging to generate power.

$$I_{\max} = j_{\mathrm{i}} A_{\mathrm{collector}} \tag{6.1}$$

$$P_{\max} = I_{\max} \Delta V \tag{6.2}$$

where j_{i} is the unperturbed ion current density and, $A_{\mathrm{collector}}$ is the surface area of the collector plate, $I_{\max}$ is the maximum current that plate can collect, and ΔV is the difference in surface potential in front of and behind the obstacle.

This setup is representative of something that could be constructed on the surface of the Moon around the rim of a crater. The value of this concept is its simplicity; it is two conducting surfaces connected by a wire. This could make a very reliable backup, or a useful start-up power supply that could be deployed while a solar panel or nuclear reactor is under construction.

Also, an interesting phenomena was observed during this demo. In the demo two LEDs were wired with opposite polarities. The expected result was that when only the neutralizer was on one LED would produce light, and when the ion source was turned on the other LED would turn on and the first would turn off. As expected, when only the neutralizer was on, only one LED produced light. When the ion beam was turned on the other light began emitting very brightly, but the other did not turn off. Instead the first LED's output began oscillating. A good next step for the GPDL would be to assess the viability of this concept with more rigor and attempt to answer the following questions: Why did the first LED not turn off as expected? What collector area is required for this concept have a meaningful power output? What impact does the presence of dust have on this concept?

Another avenue of experimentation that could have an immediate impact on the community researching dusty plasma is CEX ion mitigation. A concept that may be worth further investigation is a screen placed upstream of a test article with apertures and wire thickness sized to absorb CEX ions but let beam ions flow through relatively unperturbed, perhaps using a magnetic field downstream of the screen to collimate them if need be. This is possible because slow moving ions create a much thicker sheath than fast moving ions. This would be beneficial because the only CEX ions present would be those locally generated.

Alternatively, the GPDL could look into adapting the electric propulsion community's method of accounting for CEX ions to our application. This would mean extrapolating the CEX ion density to zero instead of background pressure. The procedure would

appear to similar; repeat experimentation at different pressures. However, in practice this could become very complex because the plasma properties need to be held constant instead of the source's operating conditions. Also, validating this method would be very difficult, likely requiring intense collaboration between the experimental and simulation teams within the GPDL.

Finally, the GPDL can experimentally verify the CEX ion density model developed in Section 5 using an RPA and propagate uncertainty from probe data and tank pressure through the calculations, along with simulations and high fidelity models.

6.3.2. Facility Upgrade Suggestions. Another important topic within future work is continuous facility improvement. This is at risk of being overlooked, but its very important to continue producing meaningful research. There are two easy ways this could be done without purchasing expensive new hardware. The first is to get more probes working. The Langmuir and Faraday probes are very useful but an RPA will allow direct measurement of the relative CEX ion density. Also, an emissive probe will be a useful tool because it will directly measure plasma potential, and, with the use of cross calibration as discussed in Section 4, may reduce uncertainty. Also, a means of obtaining time-resolved data will be valuable. For example, a triple probe or a high speed null probe as presented in [21] could provide profiles of electron temperature and density vs. time. This will allow the GPDL to investigate the transition between different plasma conditions. This is a topic of interest in the dust mitigation community, the need for which was discussed at the 2020 LPI Lunar Dust Workshop.

Another thing that could be done easily with significant long-term benefit is to add to the performance maps presented in Section 4. As they are presented in this document they are fairly sparse, only including the 16 test points provided by Veeco® . The usefulness of these maps will be improved with more points within the operational envelope included. Dedicated experimentation may not be required for this, the maps should be built upon as new points are investigated.

APPENDIX A.

FURTHER ACKNOWLEDGMENTS

Dr. Pernicka, though you aren't on my committee, you've done a lot for me for which I am very grateful. You welcomed me into the Missouri S&T Satellite Research Team (M-SAT) with open arms and gave me good advice while I was applying to graduate school. Orbits 1 and 2 were both fun and rewarding, thank you for everything.

I would also like to thank all of the supporting entities in the department and university. The machine shop and electronics shop provided valuable technical support for this work. Skyler, your welding job on the new vacuum chamber flange improved the seal compared to the previous blank plate. Lea Hickerson of the Office of Graduate Studies, thank you for the revising this thesis. You found things I would not have even thought to look for. Karen Walberg of the Mechanical and Aerospace Engineering front office, I cannot count the number of times you have sorted out administrative nightmares for me; I hope you know that everything you do is appreciated.

Also, I would like to thank Andrew Kueny, you are the one who talked me into joining M-SAT in the first place: thank you. I would still be in a field that was not right for me had we not had that conversation.

Finally, I would like to thank my parents. You supported me both emotionally and financially through my undergrad, and continued the support as I went to grad school in a new field. Switching fields, as I did, was a significant risk, and I don't think I could have gone through with it without your unwavering support. I cannot express how much I love and respect both of you.

APPENDIX B.

VACUUM CHAMBER OPERATION

1. NOMINAL OPERATION

1.1. SAFETY NOTES

To start off, there are a few safety notes about the vacuum chamber that should be noted before the procedure is discussed. Most importantly, hot diffusion pump oil cannot be exposed to atmospheric pressure. Boiling oil vapors in the presence of oxygen is a major fire hazard. Also, do not move a valve if it is under a pressure differential. The backing valve will scrape against its housing and this accelerates wear. It could also tear the O-rings on the diffusion pump valves removing their ability to seal.

Diffusion pumps 1 and 4 are known to cause problems. Pump 1 tends to overheat its oil and pump 4 tries to boil its cooling water. If either of these pumps are in operation the temperatures need to be monitored closely.

1.2. PROCEDURE

The vacuum chamber is operated through a very intuitive LabView 2019 UI called "Launch all." When it is opened two windows will open, shown in Figure 1. Figure 1a is the control panel and Figure 1b needs to be activated to access the control panel; click the right facing arrow to do so. The top section of the control panel displays the state of each valve, the tank pressure, and the pressure in the piping between the backing pump and diffusion pumps. It also displays cooling water temperature, diffusion oil temperature and the temperature of both mechanical pumps. There is a message box that will display warnings about the system.

The operating procedure is as follows:

1.2.1. Start Up.

1. Enable control

2. Open backing valve. Its display should change from red to green.

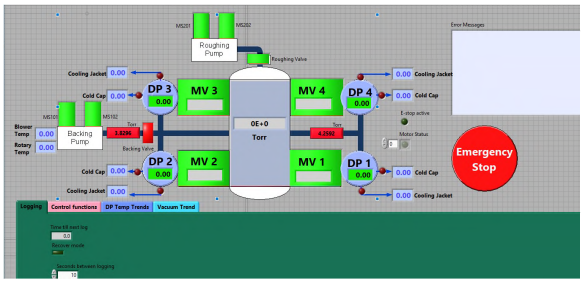

(a) Vacuum chamber control window. Click on the tabs at the bottom to switch between data storage options, the control panel, temperature trends, and vacuum trend.

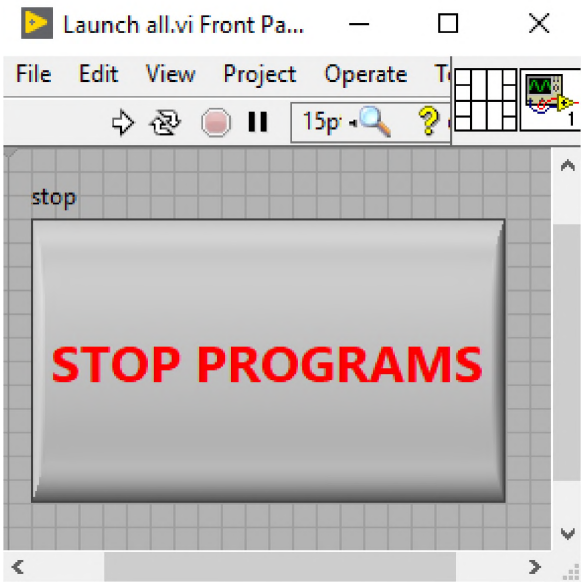

(b) Vacuum Chamber activation window.

Figure 1. Demonstration of utilizing differential charging to generate power.

3. Open the respective valve for the diffusion pump(s) to be used. If diffusion pumps will not be used at least one of the valves needs to be opened to allow flow through the tank.

4. Ensure the venting valve is closed (green handle on the chamber door).

5. After the valve(s) are fully opened start the backing pump. Both indicators should switch from green to red. If either indicator does not change, or if they are flashing, a fault has occurred; turn off the pump. If the pump has not been run on that day, the most likely cause is the circuit breaker, unscrew the panel on the roots blower and reset the breaker.

6. Monitor the tank pressure until it drops below 550 Torr (should take about 5 minutes). If the chamber has a substantial leak, for example if you forgot to close the venting valve, it will settle at about 600 Torr. This step is a check that the backing pumps are operating nominally.

7. When the pressure reaches below 1 Torr turn on the cooling water for the diffusion pump(s) to be used.

8. Turn on the pertinent diffusion pump(s).

9. Immediately verify that the cooling water is flowing. Step into the hallway outside the lab, you will be able to hear the cooling pump operating upstairs. Feel the copper pipes where they run along the wall, you should be able to feel water running through them. Also, after a few minutes the supply should be much cooler than the return.

10. Wait for the tank pressure to reach steady state, this will require between 1 and 3 hours depending on which pump(s) are used. Monitor oil and water temperature; if pump 1 and/or 4 are used monitor them very closely. If cooling water gets above 176 °F or if the oil temperature gets above 500 °F, turn off the pertinent pump(s) until the the temperatures drop to safe levels. It is worth mentioning that the displays are in Fahrenheit, but the trend plots read Celsius. DO NOT ALLOW COOLING WATER TO REACH BOILING (212 °F or 100°C).

11. Conduct planned experimentation.

1.2.2. Shut Down.

1. Turn off diffusion pump(s), leave cooling water on.

2. When oil in all diffusion pumps are below 170 °F close the backing valve.

3. Turn off the backing pump. Ensure the backing valve is off first. Only do this if you are done for the day. This pump will not spool up against an adverse pressure gradient. Once it is turned off it will need to equilibrate for several hours before it will work again.

4. Open the venting valve.

5. Wait until the oil temperature drops below 120 °F. Close the diffusion pump valves.

6. Turn off the cooling water to all pumps

7. Click "Stop Programs" on activation window.

2. EXTREME OPERATION

Sometimes you may need to get into the chamber without turning off the backing pump. An example of such a scenario is if a probe fails and you wish to troubleshoot it then finish experimentation in the same day. This is not a desired action, and in most scenarios it is better to accept the fact that the day has been lost. Only utilize this procedure in extreme cases where losing a day is not an option. The problem with this procedure is not safety, it is simply that in most cases it creates more hassle and stress than it is worth. The procedure is as follows:

1. Assess the situation. Is performing a nominal shutdown, fixing the problem, then conducting the experiment tomorrow an option? If it is not, why? Will it push back someone's graduation a semester? Will it cause a critical deadline to be missed? What time is it? This process could take 4 hours plus the additional 2 hours after experimentation is complete to perform a nominal shutdown. How much time will this really save compared to coming in early tomorrow morning? Has the roughing pump (underneath the chamber) gone through recent maintenance; i.e. is it in working order? How are the oil levels inside the roughing pump?

2. After Step 1 is seriously considered, and this course of action is chosen, close all diffusion pump valves.

3. Turn off the diffusion pumps. They will have plenty of time to reheat later on in this procedure without causing a delay.

4. Vent the chamber. Disable control.
5. Have someone continuously monitor the pressure in the piping between the backing pump and diffusion pumps. If it starts to rise there is a leak; skip to Step 8.
6. Do whatever work needs to be done inside the chamber.
7. Ensure that no debris is in the opening to the roughing pump. Use a shop-vac to clean the screen if needed.
8. Leave the chamber, seal the door. Enable Control.
9. Open the Roughing Valve.
10. Start Roughing Pump.
11. Turn the diffusion pump(s) back on. There is still vacuum where hot oil exists, so this is safe (unless you skipped ahead due to a leak; in that case skip this step).
12. Wait until the tank pressure is close to the pipe pressure. A perfect match is unlikely; if needed you can move on if the pressure is below 1 Torr. The roughing pump is slightly undersized for the vacuum chamber so this could take hours, especially if outgassing is significant.
13. Open the pertinent diffusion pump valves.
14. Close roughing valve.
15. Turn off roughing pump.
16. Run experiments then shutdown as normal.

3. LEAK PROOFING

For pressurized connections a leak will be outward. To check for leaks in this scenario, first slightly pressurize the gas line. If audible leaks exist, tighten the respective fittings until they stop; be cognizant of the possibility of cross-threading. Once all the audible leaks cease or if none exist use a q-tip to apply soapy water to the outside of each joint. Be sure to apply it on any point a leak may occur (the threads, the tube insert into the fitting, etc.). If the soapy water bubbles tighten the fitting until it stops. Increase pressure and recheck for leaks. Repeat until the pressure is much greater than the maximum expected operating pressure, but be sure to not exceed the pressure rating of any equipment. When done leak checking wash away the soap with a low-boiling alcohol, such as 99% isopropyl alcohol or denatured ethanol. It is worth mentioning that this system operates for hours, not days or weeks, so this procedure is good enough for the application. In the aerospace industry more rigorous leak proofing is commonly performed, for example, M-SAT's procedure leaves the fuel line pressurized and monitors it for weeks or months because that is representative of how long their equipment will need to operate.

For vacuum connections a leak will be inwards. The first step to check for leaks is to pull a vacuum in the vacuum chamber. As with above, first seal all audible leaks. Once audible leaks are sealed the remainder of this procedure will require two people. One person monitors the tank pressure while the other sprays a low-boiling alcohol into each fitting, one at a time. If a leak exists the chamber pressure will spike. Patience is key; the pressure increase takes time to travel from the leak to the pressure gauge. If alcohol is applied to the next joint too quickly then the alcohol will need to be fully evaporated and the procedure repeated to know which joint caused the spike. It is also useful to compare the chamber base pressure to what it was prior to the installation of new equipment.

APPENDIX C.

VEECO® RF PLASMA SOURCE OPERATION

1. SAFETY NOTES

Before the procedures are discussed, there are a few safety notes to cover. This is high voltage equipment, be sure that at least two people are present in the lab when working with the plasma source. A second person needs to be present to call 911 and perform CPR if someone gets electrocuted.

2. ROUGH PROCEDURE

This section is a rough procedure to operate the source. Its intention is to provide supplemental information gained by experience to complement the manuals provided by Veeco®, not to be an exhaustive set of instructions. At the very least read the NOVUS ION SOURCE CONTROLLER manual before operating the plasma source, though reading all of the supplied manuals is strongly encouraged.

2.1. PURGING THE GAS LINES

Every time the feed gas is changed the gas lines need to be purged. This should also be done periodically because of small leaks slowly contaminating the feed, though the frequency of doing so is up to the user. Doing this semesterly is an arbitrary suggestion.

1. Start up the vacuum chamber as normal. Rough vacuum is okay, so no diffusion pump operation is required.
2. Make sure the gas supply is off.
3. Plug in the flow controllers; move the set-points to their maximum.
4. Wait for flow to cease. The gas lines are now empty.
5. Unplug flow controllers, fill gas lines with the (new) feed gas. Repeat starting at Step 2 if desired. Repetitions will minimize lingering contaminates.

2.2. OPERATING PROCEDURE

2.2.1. Preparation.

1. Plug the Novus Controller into the 240 V extension that is fed through the Faraday Cage.
2. Move the switch on the back of the RF generator to "on."
3. Power on the Controller, RF Generator and Matching Network Controller. These do not need to be powered on in any particular order.
4. Plug in the flow controllers.
5. Plug in the recirculating pump. This overheats in about an hour and a half, and is the limiting factor for the source's operation. Be sure to do this last.

2.2.2. Startup.

1. Make sure everything in "Preparation" was competed.
2. Press the "Source" button on the controller touchscreen. This will initialize the automated startup procedure for the ion source.
3. The Neutralizer will activate first. There are two dials on the vacuum chamber throughput for the neutralizer. These are used to tune the impedance of the transmission line to minimize reflected power. During start up these will need to be adjusted because the neutralizer's impedance will change. Try to keep the reflected power to a minimum to minimize start up time.
4. Once neutralizer emission is established, the controller will automatically begin powering up the ion source then enter idle mode. Once idle mode is reached let the source warm up for at least 5 minutes before operating extracting a beam. If the extracted beam is flickering it means that the source needs to warm up longer. Return to idle mode and wait an additional 5 minutes.

2.2.3. Extracting a Beam.

1. Set the Beam Current, Beam Voltage, and Accelerator Voltage to the proper value. To do this depress their respective field on the touchscreen. A keypad will appear with the value displayed at the top; you may enter the new value if a change is desired.

2. Depress the "Beam" button on the touch screen. This will activate the accelerator grid and begin extracting a beam.

3. No further action is required. Periodically check the temperature displays and feel the cooling water tubing. The cooling water will warm up during normal operation, but if it gets too hot then shutdown is needed (the difference between normal heating and overheating is very obvious). Also, listen for variation in pump's sound, this could indicate an overheat as well.

4. When done, depress the "Beam" button again to return to idle mode. If you wish to investigate a new operating condition go back to Step 1 of this sequence.

2.2.4. Shutdown.

1. When finished return to idle mode.

2. Depress the "Source" button, this will turn everything off.

3. Unplug the recirculating pump and flow controllers.

4. Power down the controller, matching network controller, and RF generator.

5. Move the switch on the back of the RF generator to "off"

6. Unplug the Novus controller.

7. After the vacuum chamber is off and pressurized close the gas supply valve and vent the gas line if no use is planned for an extended period.

APPENDIX D.

MY ADVICE TO A BEGINNING RESEARCHER

1. READ MORE PAPERS EARLY

The work you are doing is rewarding, otherwise you wouldn't want to do it; it is also important, otherwise no one would fund it; finally, it is difficult, otherwise someone would have done it already. With this in mind, it is important to build up your knowledge base early in your graduate career. This will make your work in future much easier, both conducting the work and writing about it. In this section I will outline the approach I took to reading academic papers. Keep in mind that this is how it worked out for me, this is just information I think would have benefited me if I had known it when I was getting started.

Everyone will tell you to read more papers; in the following sections I make a few suggestions on how to get the most out of each paper.

1.1. LEARNING HOW TO READ ACADEMIC ARTICLES

Early on, I would suggest reading papers with the focus on learning how to read them. They are very dense with information, much more so than a textbook, and they can be intimidating to someone who isn't experienced yet. At this stage it is important to take very thorough notes on each paper you read. The purpose of this is twofold. First, it ensures active consumption of the content; academic literature can be so dense with information that important information may be missed if the reader is unaccustomed to it. Second, it gives insight into other lab's setups; most experimental work will explicitly show the setup, in some cases stating equipment by product name. This will be very helpful when shopping for new lab equipment and it is information which may have been missed otherwise. Also, look for what you like and do not like about how information is presented; this will help later on when you are writing: emulate what you liked, and avoid what you didn't. Also, at this stage it is important to read papers from a variety of topics, even if it isn't something you plan to work directly on; it is good to have familiarity with adjacent fields. You can also utilize this stage to figure out exactly what area you want to focus on.

1.2. BUILDING YOUR KNOWLEDGE BASE

There is no "fluff" or "filler" in academic journals, but there is information that needs to be said to put the work into context but doesn't contribute significantly to the main objective of the work. Once you have read enough papers to know the context of the work you can skim these sections and won't need to take thorough notes on them. This will allow you to focus on the new information each paper brings and increase the rate at which you can read papers, take advantage of this to rapidly build your knowledge base. There are a few things to be aware of at this stage. Look at the context in which papers use their references, build your queue of papers to read accordingly. This will yield much more targeted results than searching for keywords in journal databases. Also, be wary of using a single paper as the basis for a portion of your work; this is a pitfall that I had fallen into. The reason to avoid putting too much value into a single paper is twofold. First, even if a paper is directly applicable to planned experimentation, it was built upon a very large body of work conducted across decades by an entire community. It will be very difficult to properly implement the methods therein without an awareness of the body of work it was built upon. Second, the experimentation in the paper was conducted at a different lab with different hardware and capabilities. For example, Lobbia et al. [21] suggests a shunt resistance of less than 100 Ω for Langmuir probes to minimize lost information. With the equipment available to the GPDL the signal to noise ratio would be atrocious for a resistor that small.

2. IMPOSTOR SYNDROME

Very common in graduate studies is something called impostor syndrome, the fear that one unqualified to do the work they are doing or that one has made a fundamental oversight in their work that would make the whole project invalid. Another way this rears its ugly head is that it can cause people to question their intelligence. It is difficult to make

these fears go away on your own so talk to someone about it; in the GPDL we support each-other not belittle each-other. There are also counseling resources on campus, utilize them if needed. Remember, the only way to avoid questioning your abilities is to never push them to their limit; you are not any lesser for having any of these fears.

REFERENCES

[1] D. Trump, "Presidential Memorandum on Reinvigorating America's Human Space Exploration Program," *Space Policy Directive-1*, 2017.

[2] "National Space Exploration Campaign Report," *NASA*, 2018.

[3] J. L. Polansky, *Laboratory Investigations of the Near Surface Plasma Field and Charging at the Lunar Terminator*. PhD dissertation, Viterbi School of Engineering, University of Southern California, Los Angelos, CA, 2013.

[4] T. Stubbs, J. Halekas, W. Farrell, and R. Vondrak, "Lunar surface charging: A global perspective using lunar prospector data," *LPI Contributions*, vol. 1280, 08, 2005.

[5] W. M. Farrell, T. J. Stubbs, J. S. Halekas, R. M. Killen, G. T. Delory, M. R. Collier, and R. R. Vondrak, "Anticipated Electrical Environment Within Permanently Shadowed Lunar Craters," *Journal of Geophysical Research: Planets*, vol. 115, no. E3, 2010.

[6] R. E. Davies and J. R. Dennison, "Evolution of Secondary Electron Emission Characteristics of Spacecraft Surfaces," *Journal of Spacecraft and Rockets*, vol. 34, no. 4, pp. 571–574, 1997.

[7] N. C. Orger, J. R. C. Alarcon, K. Toyoda, and M. Cho, "Lunar Dust Lofting Due to Surface Electric Field and Charging Within Micro-Cavities Between Dust Grains Above the Terminator Region," *Advances in Space Research*, vol. 62, no. 4, pp. 896–911, 2018.

[8] K. Chou, A. Wang, and W. Yu, "Laboratory Investigations of Electrostatic Discharge Risks for Astronauts on Lunar Surface," in *AIAA Scitech 2019 Forum*, AIAA 2019-0058, (San Diego, California), January 2019.

[9] D. Han, J. J. Wang, and X. He, "Immersed finite element particle-in-cell simulations of plasma charging at the lunar terminator," *Journal of Spacecraft and Rockets*, vol. 55, no. 6, pp. 1490–1497, 2018.

[10] M. L. R Walker, A. L. Victor, R. R. Hofer, and A. D. Gallimore, "Effect of Backpressure on Ion Current Density Measurements in Hall Thruster Plumes," *Journal of Propulsion and Power*, vol. 21, no. 3, pp. 408–415, 2005.

[11] D. L. Brown, M. L. R. Walker, J. Szabo, W. Huang, and J. E. Foster, "Recommended practice for use of faraday probes in electric propulsion testing," *Journal of Propulsion and Power*, vol. 33, no. 3, pp. 582–613, 2017.

[12] Y. Azziz, "Instrument development and plasma measurements on a 200-watt hall thrsuter plume," Master's thesis, Department of Aeronautics and Astronautics, Massachusetts Institute of Technology, Cambridge, MA, 2003.

[13] Y. Azziz, M. Martinez-Sanchez, and J. Szabo, "Determination of in-orbit plume characteristics from laboratory measurements," in *42nd AIAA/ASME/SAE/ASEE Joint Propulsion Conference & Exhibit*, AIAA 2006-4484, (Sacramento, California), July 2006.

[14] Veeco Instruments Inc., *12 cm RF Ion Source Technical Manual*, 2002.

[15] B. Folta, T. W. McGarvey, J. C. Faudel, K. R. McMillen, and D. Han, "Development and characterization of an ion source to simulate solar wind plasma in a vacuum chamber," in *AIAA Scitech 2020 Forum*, AIAA 2020-0048, (Orlando, Florida), January 2020.

[16] *Cold cathode/Pirani gauge ACC 2009 User's Manual*, 2 ed., 2008.

[17] C. Enloe, L. H. Krause, M. G. McHarg, O. Nava, P. Shoemaker, E. Ehmann, and J. Williams, "Characterization of a plasma source for ground-based simulation of leo plasma conditions," in *2nd International Energy Conversion Engineering Conference*, AIAA 2004-5668, (Providence, Rhode Island), August 2004.

[18] J. Polansky, J. Wang, and N. Ding, "Experimental Investigation on Plasma Plume Potential," *IEEE Transactions on Plasma Science*, vol. 41, pp. 3438–3447, 12, 2013.

[19] J. D. Frieman, J. A. Walker, M. L. R. Walker, V. Khayms, and D. Q. King, "Electrical Facility Effects on Hall Thruster Cathode Coupling: Performance and Plume Properties," *Journal of Propulsion and Power*, vol. 32, no. 1, pp. 251–264, 2016.

[20] N. Hershkowitz, "3 - How Langmuir Probes Work," in *Plasma Diagnostics* (O. Auciello and D. L. Flamm, eds.), pp. 113 – 183, Academic Press, 1989.

[21] R. B. Lobbia and B. E. Beal, "Recommended Practice for Use of Langmuir Probes in Electric Propulsion Testing," *Journal of Propulsion and Power*, vol. 33, no. 3, pp. 566–581, 2017.

[22] G. Narasimhan and C. Steinbrüchel, "Analysis of Langmuir Probe Data: Analytical Parametrization, and the Importance of the End Effect," *Journal of Vacuum Science and Technology A*, vol. 19, pp. 376–378, 01, 2001.

[23] A. Shabshelowitz and A. D. Gallimore, "Performance and Probe Measurements of a Radio-Frequency Plasma Thruster," *Journal of Propulsion and Power*, vol. 29, no. 4, pp. 919–929, 2013.

[24] B. Cherrington, "The Use of Electrostatic Probes for Plasma Diagnostics-A Review," *Plasma Chemistry and Plasma Processing*, vol. 2, no. 2, pp. 113–140, 1982.

[25] R. B. Lobbia and A. D. Gallimore, "High-Speed Dual Langmuir Probe," *Review of Scientific Instruments*, vol. 81, no. 7, p. 073503, 2010.

[26] J. Wang, J. Brophy, D. Brinza, J. Wang, J. Brophy, and D. Brinza, "A Global Analysis of Ion Thruster Plume Interactions for Interplanetary Spacecraft," in *33rd Joint Propulsion Conference and Exhibit*, AIAA 97-3194, (Seattle, Washington), July 1997.

[27] H. Martínez, F. Castillo, P. Reyes, and F. Santibañez, "Experimental Studies on the Formation of Argon Atoms in Ar+ -Atoms Collisions," *International Journal of Mass Spectrometry*, vol. 228, pp. 107–116, 08 2003.

[28] G. Soulas, "Modeling neutral densities downstream of a gridded ion thruster," in *46th AIAA/ASME/SAE/ASEE Joint Propulsion Conference & Exhibit*, AIAA 2010-6699, (Nashville, Tennessee), July 2010.

[29] J. V. Noord, "Next ion thruster thermal model," in *43rd AIAA/ASME/SAE/ASEE Joint Propulsion Conference & Exhibit*, AIAA 2007-5218, (Cincinnati, OH), July 2007.

[30] J. Foster, G. Soulas, and M. Patterson, "Plume and discharge plasma measurements of an NSTAR-type ion thruster," in *36th AIAA/ASME/SAE/ASEE Joint Propulsion Conference and Exhibit*, AIAA 2000-3812, (Las Vegas, Nevada), July 2000.

VITA

Blake Anthony Folta was born in 1995 in St. Louis, Missouri. In August of 2013 he began his collegiate career at Missouri University of Science and Technology. As an undergraduate he was an active member of Sigma Pi Fraternity International, for which he held several leadership positions including Secretary and Scholarship Committee Chairman. He graduated Cum Laude with a Bachelors of Science degree in Chemical Engineering in December of 2017. At the beginning of his graduating semester a Fraternity brother convinced him to join the Missouri S&T Satellite Research Team (M-SAT), which catalyzed his decision to pursue a Masters of Science degree in Aerospace Engineering in the field of plasma dynamics. He began conducting experimental research in the field under Dr. Han in the Gas and Plasma Dynamics Lab (GPDL) the following spring. In December of 2020 he received his masters degree in Aerospace Engineering from Missouri University of Science and Technology, and has since moved on to begin his professional career at Eglin Air Force Base, FL.